SOLUTION-PROCESSED LEAD-FREE PIEZOELECTRIC MATERIALS AND DEVICES

Rajinder Singh Deol

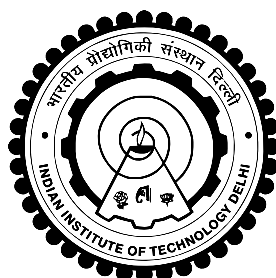

DEPARTMENT OF ELECTRICAL ENGINEERING

INDIAN INSTITUTE OF TECHNOLOGY DELHI

March 2022

©Indian Institute of Technology Delhi (IITD), New Delhi, 2022

All rights reserved.

Solution-processed lead-free piezoelectric materials and devices

A doctoral dissertation

By

Rajinder Singh Deol (ID: 2013EEZ8532)

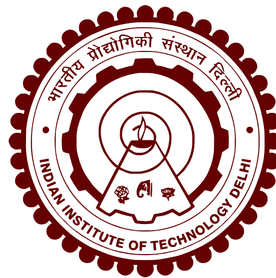

Submitted in partial fulfilment of the requirements for the degree of Doctor of Philosophy

at

Indian Institute of Technology Delhi

March 2022

Copyright © 2022 Rajinder Singh Deol All Rights Reserved, except for any material that may be clearly marked and attributed to external sources. In those cases alone, the copyrights pertaining to the identified material belong to their respective owners.

Use of the material herein is protected by Indian Copyright Act, 1957 (and any subsequent Amendments), and applicable International copyright Treaties that India is signatory to. "Fair Use" and "fair dealing" is permitted within the context of widely accepted academic standards, subject to legal interpretation in Indian courts.

The author(s) hereby grant(s) to IIT Delhi permission to reproduce, and to distribute publicly, paper and electronic copies of this document using any medium now known, or hereafter created, subject to conditions of the copyright, and reproduction of this notice.

Certificate from Advisor(s)

This is to certify that the thesis entitled **Solution-processed lead-free piezoelectric materials and devices**, being submitted by **Rajinder Singh Deol** to IIT Delhi, is worthy of consideration for the award of the degree of **Doctor of Philosophy** and is a record of the original research work carried out by this student under my/our supervision. The results contained in this thesis, which may have been previously communicated in the form of manuscripts, conference presentations or patent filings, have not been submitted in part or full, to any other University or Institute for the award of any academic degree.

I/We certify that this student has pursued the prescribed course of research.

Research Advisor (s):

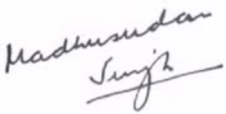

Madhusudan Singh[1]

[1]Department of Electrical Engineering, IIT Delhi

Acknowledgements

I want to express my sincere gratitude towards my supervisor Prof. Madhusudan Singh for his valuable support and mentor during this unusual journey. I want to thank him for providing multiple opportunities to attend international conferences. I want to thank Prof. Bhaskar Mitra, Prof. B. Bhaumik, and Prof. R. Shankar for their valuable inputs during the PhD as my SRC. Special thanks to Prof. R. Shankar for helping me during my initial journey stages and extending his full support to make my life a little less challenging. He opened the doors of his lab and allowed me to work in his lab when I had no place to run my experiments. This gesture is beyond professionalism and is pure humanitarian. I would also thank Prof. Ghassan Jabbour and Prof. J. Park for hosting me at the University of Ottawa, which allowed me to explore cleanroom CMOS fabrication and Ottawa. A huge thanks to the on-campus central facilities such as CRF, NRF, and their managing staff. I am also grateful to Mr. Satish and Mr. Yatindra (staff of Department of Electrical Engg.) who helped in all kinds of official paperwork.

I want to thank my labmates (FMDL) Ms. Nitika Batra, Mr. Pranjal Rai, Ms. Kritika Bhattacharya, Ms. Harpreet Kaur, Dr. Meenal Mehra, Dr. Soumen Saha, and Dr. Sylvia Devi for helping and contributing (directly/indirectly) in my experiments. Equally important are the others (FMDL) who helped around the lab and for things such as lab development etc. that are beyond the scope of this acknowledgement.

I also want to thank Mr. Anthony Olivieri, Ms. Chelsea Barna, Mr. Howard Northfield, and Mr. Shobhit Kareer for their help and support during my stay at the University of Ottawa. I am equally thankful to Mr. Robert Vandusen, Mr. Rodney Aiton, and Ms. Angela Williams for helping me in the fabrication process at Carleton University.

I am extremely indebted to Mr. Shashank Sharma, Dr. Anuj, Mr. Nardev Bajaj, Mr. Hardeep Singh, Dr. Aditya Gokhale, Mr. Jakson, Mr. Jaskirat Singh, Mr. Gurinder Singh, Mr. Ripudaman Singh, Mr. Paramvir Singh, Mr. Akaljot Singh, and Mr. Arvinder Singh for their comradery and support during tough times. They not only helped me with access to their lab equipment, facilities, and other favors but have also taught me

things in general.

I also want to thank Prof. Shouri Chatterjee (EE), Prof. Naresh Datla (ME), and Prof. S. P. Singh (ME) for their support during energy harvesting and LDV experimentation. I am grateful for Ministry of Human Resources & Development (MHRD) and IITD for financial support during this journey and SPARC fellowship.

I am incredibly grateful for having a tremendous friend circle and for their unwavering support during this journey.

I can never forget the sacrifice of my family, especially my wife Nitika, who supported me in all conditions, for better or for worse. They not only tolerated me but my behaviour and my absence on many important occasions. Their patience cannot be underestimated and should not be left unrecognized. They also provided financial supports whenever needed without asking and cleverly disguised as blessings.

Finally, I am grateful to the almighty for making Ibadat (my niece) a part of our family, who came into our lives in the difficult times of COVID-19. Her mere presence in our lives made tough times easy.

Abstract

Sensors, actuators, transducers in micro-electromechanical systems (MEMS), technologies using micro-optical devices such as atomic force microscopes (AFM), infrared (IR) detector arrays etc., are used to connect mechanical changes with changes in the charge state of the active piezoelectric layer. For ubiquitous deployment of MEMS-based vibration energy harvesters in distributed flexible sensors, fabrication processes must be cost-effective and environmentally friendly. Lead zirconium titanate (PZT) and other lead-based materials such as lanthanum-doped PZT (PLZT), $Pb(Mg_{1/3}Nb_{2/3})O_3$ $PbTiO_3$ (PMN-PT) dominate the market for piezoelectric materials due to their excellent electromechanical properties. However, the presence of lead in these materials presents an environmental and health challenge that limits the regulatory approval for several devices. Within the overall history of electrically active ceramics, technological interest in the perovskite potassium sodium niobate ($K_xNa_{1-x}(NbO_3)$ KNN) has grown over the previous decade due to the high electromechanical coefficients (d_{33}). The performance of KNN compares favourably with the performance of industrially relevant but environmentally deprecated materials composed of lead perovskites like PZT, PMN-PT, etc.

This dissertation focuses on the synthesis and deposition process for fabricating uniform amorphous thin (∼ 70 nm) unannealed films of potassium sodium niobate (KNN). This study employed three different ratios of sodium and potassium in order to study the stoichiometric effects of composition on the final film and its piezoelectric properties. The study focuses on reducing the overall thermal budget of processing from materials synthesis to fabrication of the device. This PhD aimed to explore and employ lead-free piezo-active material to fabricate flexible devices such as energy harvesters. The low thermal footprint of the process is likely to significantly lower the cost of devices requiring high-performance piezoelectric materials, which are also environmentally friendly. The impact of electric-field assisted densification of a low temperature solution-processed piezoelectric inorganic film (potassium sodium niobate, KNN) has also been investigated. A concentrated ($K_xNa_{1-x}(NbO_3)$, x=0.5) sol of the material was drop casted on an insulating SiO_2 substrate with two electrodes deposited in a lateral diode geometry. Surface metrology and compositional scans on the

post-processed film revealed a cracked morphology with apparent densification and a stoichiometric shift from 51:49 to 31:69 (K:Na). An image processing method was used on electron microscopy images to estimate a ~20 % volume reduction over an area of 400 μm^2 using topographical film data. Further, the system was simulated using a finite element method on a 3D model system, and the simulated electric field lines appear to explain the observed post-annealed densified profiles.

A modified method for the estimation of electromechanical coefficient (d_{33}) of thin film has been developed for the characterization of a solution-processed piezoceramic thin-film $M\pi M$ parallel-plate capacitor structure using capacitance-voltage measurements. Electrical loading was applied to the capacitor to stimulate out-of-plane longitudinal and transverse elongation. The results were validated using FEM-based modelling and compared with several measurements in literature, including piezoresponse force microscopy-based measurements, which are generally considered unreliable due to strong electrostatic interactions between the tip-cantilever, and the charged sample surface, wherein such artefacts result in the overestimation of the electromechanical response of the material under investigation.

Further, a metal-piezo-metal (MπM) based single-pixel (sensing element or energy harvester) 1x1 cm energy harvester was fabricated using solution-processed potassium sodium niobate films on aluminium-coated polyethylene terephthalate (PET) substrates. Initial measurements using a full-wave diode bridge rectifier circuit show a real-time response time of (~0.13 sec) on the application of variable pressure. The magnitude of the voltage signal generated is $\sim$ 40 mV greater than the expected rectification drop of $\sim$ 1.4 V, suggesting significant charge transduction in the harvester.

In summary, in the course of the doctoral work, material development, material characterization, device design, device fabrication, and characterization involving solution-processed lead-free materials have been carried out.

सार

माइक्रो–इलेक्ट्रोमैकेनिकल सिस्टम (MEMS) में सेंसर, एक्ट्यूएटर, ट्रांसड्यूसर, माइक्रो–ऑप्टिकल डि–वाइस जैसे परमाणु बल माइक्रोस्कोप (AFM), इन्फ्रारेड (आईआर) डिटेक्टर एरे इत्यादि का उपयोग करने वाली प्रौद्योगिकियों का उपयोग चार्ज स्थिति में परिवर्तन के साथ यांत्रिक परिवर्तनों को जोड़ने के लिए किया जाता है। सक्रिय पीजोइलेक्ट्रिक परत की। वितरित लचीले सेंसर में एमईएमएस–आधारित कंपन ऊर्जा हा–र्वेस्टर की सर्वव्यापी तैनाती के लिए, निर्माण प्रक्रिया लागत प्रभावी और पर्यावरण के अनुकूल होनी चाहिए। लेड जिरकोनियम टाइटेनेट (PZT) और अन्य लेड–आधारित सामग्री जैसे लैंथेनम–डॉप्ड PZT (PLZT), $Pb(Mg_{1/3}Nb_{2/3})O_3$ $PbTiO_3$ (PMN–PT) पीजोइलेक्ट्रिक सामग्री के लिए बाजार पर हावी हैं। उत्कृष्ट वि–द्युत यांत्रिक गुण। हालांकि, इन सामग्रियों में लेड की उपस्थिति एक पर्यावरण और स्वास्थ्य चुनौती प्रस्तुत करती है जो कई उपकरणों के लिए नियामक अनुमोदन को सीमित करती है। विद्युत रूप से सक्रिय सिरेमिक के समग्र इतिहास के भीतर, पेरोसाइट पोटेशियम सोडियम नाइओबेट ($K_xNa_{(1-x)}(NbO_3)$, KNN) में तकनीकी रुचि पिछले एक दशक में उच्च इलेक्ट्रोमैकेनिकल गुणांक (d_{33}) के कारण बढ़ी है।. KNN का प्रदर्शन औद्योगिक रूप से प्रासंगिक लेकिन पर्यावरणीय रूप से बहिष्कृत सामग्री जैसे पीजेडटी (PZT), पीएमएन–पीटी (PMN–PT), आदि जैसे लीड पेरोव्स्काइट्स के प्रदर्शन के साथ अनुकूल रूप से तुलना करता है।ुलना करता है। है।

यह शोध प्रबंध पोटेशियम सोडियम नाइओबेट (KNN) की एकसमान अनाकार पतली ($\sim$ 70 nm) अनावृत फिल्मों के निर्माण के लिए संश्लेषण और निक्षेपण प्रक्रिया पर केंद्रित है। इस अध्ययन ने अंतिम फिल्म और इसके पीजोइलेक्ट्रिक गुणों पर संरचना के स्टोइकोमेट्रिक प्रभावों का अध्ययन करने के लिए सोडियम (Na) और पोटेशियम (K) के तीन अलग–अलग अनुपातों को नियोजित किया। अध्ययन सामग्री संश्लेषण से उपकरण के निर्माण तक प्रसंस्करण के समग्र थर्मल बजट को कम करने पर केंद्रित है। इस पीएचडी का उद्देश्य ऊर्जा हार्वेस्टर जैसे लचीले उपकरणों को बनाने के लिए सीसा रहित पीजो–सक्रिय सामग्री का पता लगाना और नियोजित करना है। प्रक्रिया के कम तापीय पदचिह्न से उच्च–प्रदर्शन पीजोइलेक्ट्रिक सामग्री की आवश्यकता वाले उपकरणों की लागत में काफी कमी आने की संभावना है, जो पर्यावरण के अनुकूल भी हैं। कम तापमान समाधान–संसाधित पीजोइलेक्ट्रिक अकार्बनिक फिल्म (पोटेशियम सोडियम नाइओबेट, केएनएन) के विद्युत–क्षेत्र सहायता प्राप्त घनत्व के प्रभाव की भी जांच की गई है। सामग्री का एक सांद्र ($K_xNa_{1-x}(NbO_3)$, $x = 0.5$) सॉल (Sol) एक इंसुलेटिंग SiO_2 सब्सट्रेट पर डाला गया था, जिसमें पार्श्व डायोड ज्यामिति में जमा दो इलेक्ट्रोड थे। पोस्ट–प्रोसेस्ड फिल्म पर सरफेस मेट्रोलॉजी और कंपोजिटल स्कैन में स्पष्ट घनत्व के साथ एक फटा आकारिकी और $51 : 49$ से $31 : 69$ ($\mathrm{K : Na}$) तक एक स्टोइकोमेट्रिक शिफ्ट का पता चला। स्थलाकृतिक फिल्म डेटा का उपयोग करके $400\,\mu m^2$ के एक क्षेत्र में $\sim 20\,\%$ मात्रा में कमी का अनुमान लगाने के लिए इलेक्ट्रॉन माइक्रोस्कोपी छवियों पर एक छवि प्रसंस्करण विधि का उपयोग किया गया था। इसके अलावा, सिस्टम को एक 3D मॉडल सिस्टम पर एक परिमित तत्व विधि का उपयोग करके सिम्युलेटेड किया गया था, और सिम्युलेटेड इलेक्ट्रिक फील्ड लाइनें मनाए गए पोस्ट–एनील्ड डेंसिफाइड प्रोफाइल की व्याख्या करती दिखाई देती हैं।

पतली फिल्म के इलेक्ट्रोमैकेनिकल गुणांक (d_{33}) के आकलन के लिए एक संशोधित विधि विकसित की गई है समाई–वोल्टेज माप का उपयोग करते हुए एक समाधान–संसाधित पाइज़ोसेरामिक पतली–फिल्म $M\pi M$ समानांतर–प्लेट संधारित्र संरचना के लक्षण वर्णन के लिए। विमान से बाहर अनुदैर्ध्य और अनुप्रस्थ बढ़ाव को प्रोत्साहित करने के लिए संधारित्र पर विद्युत लोडिंग लागू की गई थी। परिणामों को फेम–आधारित मॉडलिंग का उपयोग करके मान्य किया गया था और साहित्य में कई मापों के साथ तुलना की गई थी, जिसमें पीज़ोरेस्पोन्स बल माइक्रोस्कोपी–आधारित माप शामिल हैं, जिन्हें आमतौर पर टिप–ब्रैकट और चार्ज नमूना सतह के बीच

मजबूत इलेक्ट्रोस्टैटिक इंटरैक्शन के कारण अविश्वसनीय माना जाता है, जिसमें ऐसी कलाकृतियां जांच के तहत सामग्री की विद्युत यांत्रिक प्रतिक्रिया के अधिक आकलन में परिणाम।

इसके अलावा, एल्युमिनियम–लेपित पॉलीइथाइलीन टेरेफ्थेलेट (पीईटी) पर समाधान–संसाधित पोटेशियम सोडियम नाइओबेट फिल्मों का उपयोग करके एक धातु–पीजो–धातु ($M\pi M$) आधारित सिंगल–पिक्सेल (सेंसिंग तत्व या ऊर्जा हार्वेस्टर) $1x1$ सेमी ऊर्जा हार्वेस्टर का निर्माण किया गया था। सब्सट्रेट। फुल–वेव डायोड ब्रिज रेक्टिफायर सर्किट का उपयोग करते हुए प्रारंभिक माप चर दबाव के आवेदन पर ($\sim$0.13 sec) का वास्तविक समय प्रतिक्रिया समय दिखाते हैं। उत्पन्न वोल्टेज सिग्नल का परिमाण $\sim 40\,\mathrm{mV}$ तथा $\sim 1.4\,\mathrm{V}$ के अपेक्षित सुधार ड्रॉप से अधिक है, जो हार्वेस्टर में महत्वपूर्ण चार्ज ट्रांसडक्शन का सुझाव देता है।।

संक्षेप में, डॉक्टरेट के काम के दौरान, सामग्री विकास, सामग्री लक्षण वर्णन, उपकरण डिजाइन, उपकरण निर्माण, और समाधान–संसाधित सीसा रहित सामग्री को शामिल करते हुए लक्षण वर्णन किया गया है।

ਸਾਰ

ਸੂਚਕ, ਐਕਚੁਏਟਰ, ਮਾਈਕ੍ਰੋ–ਇਲੈਕਟਰੋਮੈਕਨੀਕਲ ਸਿਸਟਮ (MEMS) ਵਿੱਚ ਟਰਾਂਸਡਿਊਸਰ, ਮਾਈਕ੍ਰੋ–ਆਪਟੀਕਲ ਯੰਤਰਾਂ ਜਿਵੇਂ ਕਿ ਐਟਮਿਕ ਫੋਰਸ ਮਾਈਕ੍ਰੋਸਕੋਪ (AFM), ਇਨਫਰਾਰੈੱਡ (IR) ਡਿਟੈਕਟਰ ਐਰੇ ਆਦਿ ਦੀ ਵਰਤੋਂ ਕਰਨ ਵਾਲੀਆਂ ਤਕਨੀਕਾਂ ਨੂੰ ਚਾਰਜ ਅਵਸਥਾ ਵਿੱਚ ਤਬਦੀਲੀਆਂ ਨਾਲ ਮਕੈਨੀਕਲ ਤਬਦੀਲੀਆਂ ਨਾਲ ਜੋੜਨ ਲਈ ਵਰਤਿਆ ਜਾਂਦਾ ਹੈ। ਸਰਗਰਮ ਪੀਜ਼ੋਇਲੈਕਟ੍ਰਿਕ ਪਰਤ ਦਾ. ਵਿਤਰਿਤ ਲਚਕਦਾਰ ਸੈਂਸਰਾਂ ਵਿੱਚ MEMS–ਅਧਾਰਤ ਵਾਈਬ੍ਰੇਸ਼ਨ ਐਨਰਜੀ ਹਾਰਵੈਸਟਰ ਦੀ ਸਰਵ ਵਿਆਪਕ ਤੈਨਾਤੀ ਲਈ, ਨਿਰਮਾਣ ਪ੍ਰਕਿਰਿਆਵਾਂ ਲਾਗਤ–ਪ੍ਰਭਾਵਸ਼ਾਲੀ ਅਤੇ ਵਾਤਾਵਰਣ ਅਨੁਕੂਲ ਹੋਣੀਆਂ ਚਾਹੀਦੀਆਂ ਹਨ। ਲੀਡ ਜ਼ਿਰਕੋਨਿਅਮ ਟਾਈਟਨੇਟ (PZT) ਅਤੇ ਹੋਰ ਲੀਡ–ਆਧਾਰਿਤ ਸਮੱਗਰੀ ਜਿਵੇਂ ਕਿ ਲੈਂਥਨਮ–ਡੋਪਡ PZT (PLZT), $Pb(Mg_{1/3}Nb_{2/3})O_3$ $PbTiO_3$ (PMN-PT) ਆਪਣੇ ਕਾਰਨ ਪੀਜ਼ੋਇਲੈਕਟ੍ਰਿਕ ਸਮੱਗਰੀ ਲਈ ਮਾਰਕੀਟ ਵਿੱਚ ਹਾਵੀ ਹਨ। ਸ਼ਾਨਦਾਰ ਇਲੈਕਟ੍ਰੋਮੈਕਨੀਕਲ ਵਿਸ਼ੇਸ਼ਤਾਵਾਂ. ਹਾਲਾਂਕਿ, ਇਹਨਾਂ ਸਮੱਗਰੀਆਂ ਵਿੱਚ ਲੀਡ ਦੀ ਮੌਜੂਦਗੀ ਇੱਕ ਵਾਤਾਵਰਣ ਅਤੇ ਸਿਹਤ ਚੁਣੌਤੀ ਪੇਸ਼ ਕਰਦੀ ਹੈ ਜੋ ਕਈ ਡਿਵਾਈਸਾਂ ਲਈ ਰੈਗੂਲੇਟਰੀ ਪ੍ਰਵਾਨਗੀ ਨੂੰ ਸੀਮਿਤ ਕਰਦੀ ਹੈ। ਇਲੈਕਟ੍ਰਿਕਲੀ ਐਕਟਿਵ ਵਸਰਾਵਿਕਸ ਦੇ ਸਮੁੱਚੇ ਇਤਿਹਾਸ ਦੇ ਅੰਦਰ, ਉੱਚ ਇਲੈਕਟ੍ਰੋਮਕੈਨੀਕਲ ਗੁਣਾਂ (d_{33}) ਦੇ ਕਾਰਨ ਪਿਛਲੇ ਦਹਾਕੇ ਵਿੱਚ ਪੈਰੋਵਸਕਾਈਟ ਪੋਟਾਸ਼ੀਅਮ ਸੋਡੀਅਮ ਨਿਓਬੇਟ ($K_xNa_{1--x}(NbO_3)$ KNN) ਵਿੱਚ ਤਕਨੀਕੀ ਦਿਲਚਸਪੀ ਵਧੀ ਹੈ।). KNN ਦੀ ਕਾਰਗੁਜ਼ਾਰੀ PZT, PMN-PT, ਆਦਿ ਵਰਗੇ ਲੀਡ ਪੇਰੋਵਸਕਾਈਟਸ ਨਾਲ ਬਣੀ ਉਦਯੋਗਿਕ ਤੌਰ 'ਤੇ ਢੁਕਵੀਂ ਪਰ ਵਾਤਾਵਰਣ ਲਈ ਨਾਪਸੰਦ ਸਮੱਗਰੀ ਦੇ ਪ੍ਰਦਰਸ਼ਨ ਨਾਲ ਅਨੁਕੂਲਤਾ ਨਾਲ ਤੁਲਨਾ ਕਰਦੀ ਹੈ।

ਇਹ ਖੋਜ ਨਿਬੰਧ ਪੋਟਾਸ਼ੀਅਮ ਸੋਡੀਅਮ ਨਿਓਬੇਟ (KNN) ਦੀਆਂ ਇਕਸਾਰ ਅਮੋਰਫਸ ਪਤਲੀ (~ 70 nm) ਅਣ–ਅਨਲਾਈਨ ਫਿਲਮਾਂ ਨੂੰ ਬਣਾਉਣ ਲਈ ਸੰਸਲੇਸ਼ਣ ਅਤੇ ਜਮ੍ਹਾ ਕਰਨ ਦੀ ਪ੍ਰਕਿਰਿਆ 'ਤੇ ਕੇਂਦ੍ਰਤ ਹੈ। ਅੰਤਮ ਫਿਲਮ ਅਤੇ ਇਸਦੇ ਪਾਈਜ਼ੋਇਲੈਕਟ੍ਰਿਕ ਵਿਸ਼ੇਸ਼ਤਾਵਾਂ 'ਤੇ ਰਚਨਾ ਦੇ ਸਟੋਈਚਿਓਮੈਟ੍ਰਿਕ ਪ੍ਰਭਾਵਾਂ ਦਾ ਅਧਿਐਨ ਕਰਨ ਲਈ ਇਸ ਅਧਿਐਨ ਨੇ ਸੋਡੀਅਮ ਅਤੇ ਪੋਟਾਸ਼ੀਅਮ ਦੇ ਤਿੰਨ ਵੱਖ–ਵੱਖ ਅਨੁਪਾਤ ਨੂੰ ਨਿਯੁਕਤ ਕੀਤਾ। ਅਧਿਐਨ ਸਮੱਗਰੀ ਸੰਸਲੇਸ਼ਣ ਤੋਂ ਲੈ ਕੇ ਡਿਵਾਈਸ ਦੇ ਨਿਰਮਾਣ ਤੱਕ ਪ੍ਰੋਸੈਸਿੰਗ ਦੇ ਸਮੁੱਚੇ ਥਰਮਲ ਬਜਟ ਨੂੰ ਘਟਾਉਣ 'ਤੇ ਕੇਂਦ੍ਰਤ ਕਰਦਾ ਹੈ। ਇਸ ਪੀਐਚਡੀ ਦਾ ਉਦੇਸ਼ ਊਰਜਾ ਵਾਢੀ ਕਰਨ ਵਾਲੇ ਲਚਕੀਲੇ ਯੰਤਰਾਂ ਨੂੰ ਬਣਾਉਣ ਲਈ ਲੀਡ–ਮੁਕਤ ਪਾਈਜ਼ੋ–ਐਕਟਿਵ ਸਮੱਗਰੀ ਦੀ ਪੜਚੋਲ ਕਰਨਾ ਅਤੇ ਰੁਜ਼ਗਾਰ ਦੇਣਾ ਹੈ। ਪ੍ਰਕਿਰਿਆ ਦੇ ਘੱਟ ਥਰਮਲ ਫੁਟਪ੍ਰਿੰਟ ਉੱਚ–ਪ੍ਰਦਰਸ਼ਨ ਵਾਲੀ ਪੀਜ਼ੋਇਲੈਕਟ੍ਰਿਕ ਸਮੱਗਰੀ ਦੀ ਲੋੜ ਵਾਲੇ ਉਪਕਰਣਾਂ ਦੀ ਲਾਗਤ ਨੂੰ ਮਹੱਤਵਪੂਰਨ ਤੌਰ 'ਤੇ ਘੱਟ ਕਰਨ ਦੀ ਸੰਭਾਵਨਾ ਹੈ, ਜੋ ਵਾਤਾਵਰਣ ਦੇ ਅਨੁਕੂਲ ਵੀ ਹਨ। ਘੱਟ ਤਾਪਮਾਨ ਦੇ ਘੋਲ–ਪ੍ਰੋਸੈਸਡ ਪਾਈਜ਼ੋਇਲੈਕਟ੍ਰਿਕ ਅਕਾਰਗਨਿਕ ਫਿਲਮ (ਪੋਟਾਸ਼ੀਅਮ ਸੋਡੀਅਮ ਨਿਓਬੇਟ, ਕੇਐਨਐਨ) ਦੇ ਇਲੈਕਟ੍ਰਿਕ–ਫੀਲਡ ਅਸਿਸਟਡ ਡੈਨਸੀਫਿਕੇਸ਼ਨ ਦੇ ਪ੍ਰਭਾਵ ਦੀ ਵੀ ਜਾਂਚ ਕੀਤੀ ਗਈ ਹੈ। ਸਮਗਰੀ ਦਾ ਇੱਕ ਕੇਂਦਰਿਤ ($K_xNa_{1--x}(NbO_3)$, x=0.5) ਸੋਲ ਨੂੰ ਇੱਕ ਇਨਸੁਲੇਟਿੰਗ SiO_2 ਸਬਸਟਰੇਟ 'ਤੇ ਸੁੱਟਿਆ ਗਿਆ ਸੀ ਜਿਸ ਵਿੱਚ ਦੋ ਇਲੈਕਟ੍ਰੋਡਾਂ ਨੂੰ ਲੈਟਰਲ ਡਾਇਓਡ ਜਿਓਮੈਟਰੀ ਵਿੱਚ ਜਮ੍ਹਾ ਕੀਤਾ ਗਿਆ ਸੀ। . ਪੋਸਟ–ਪ੍ਰੋਸੈਸਡ ਫਿਲਮ 'ਤੇ ਸਰਫੇਸ ਮੈਟਰੋਲੋਜੀ ਅਤੇ ਕੰਪੋਜੀਸ਼ਨਲ ਸਕੈਨਾਂ ਨੇ ਸਪੱਸ਼ਟ ਘਣਤਾ ਅਤੇ 51:49 ਤੋਂ 31:69 (K:Na) ਤੱਕ ਇੱਕ ਸਟੋਈਚਿਓਮੈਟ੍ਰਿਕ ਸ਼ਿਫਟ ਦੇ ਨਾਲ ਇੱਕ ਕ੍ਰੈਕਡ ਰੂਪ ਵਿਗਿਆਨ ਦਾ ਖੁਲਾਸਾ ਕੀਤਾ। ਟੌਪੋਗ੍ਰਾਫਿਕਲ ਫਿਲਮ ਡੇਟਾ ਦੀ ਵਰਤੋਂ ਕਰਦੇ ਹੋਏ $400\,\mu m^2$ ਦੇ ਖੇਤਰ ਵਿੱਚ $\sim 20\,\%$ ਵਾਲੀਅਮ ਕਮੀ ਦਾ ਅੰਦਾਜ਼ਾ ਲਗਾਉਣ ਲਈ ਇਲੈਕਟ੍ਰੋਨ ਮਾਈਕ੍ਰੋਸਕੋਪੀ ਚਿੱਤਰਾਂ 'ਤੇ ਇੱਕ ਚਿੱਤਰ ਪ੍ਰੋਸੈਸਿੰਗ ਵਿਧੀ ਵਰਤੀ ਗਈ ਸੀ। ਅੱਗੇ, ਸਿਸਟਮ ਨੂੰ ਇੱਕ 3D ਮਾਡਲ ਸਿਸਟਮ 'ਤੇ ਇੱਕ ਸੀਮਿਤ ਤੱਤ ਵਿਧੀ ਦੀ ਵਰਤੋਂ ਕਰਕੇ ਸਿਮੂਲੇਟ ਕੀਤਾ ਗਿਆ ਸੀ, ਅਤੇ ਸਿਮੂਲੇਟਿਡ ਇਲੈਕਟ੍ਰਿਕ ਫੀਲਡ ਲਾਈਨਾਂ ਦੇਖਿਆ ਗਿਆ ਪੋਸਟ–ਐਨੀਲਡ ਡੈਨਸਫਾਈਡ ਪ੍ਰੋਫਾਈਲਾਂ ਦੀ ਵਿਆਖਿਆ ਕਰਨ ਲਈ ਦਿਖਾਈ ਦਿੰਦੀਆਂ ਹਨ।

ਪਤਲੀ ਫਿਲਮ ਦੇ ਇਲੈਕਟ੍ਰੋਮਕੈਨੀਕਲ ਗੁਣਾਂਕ (d_{33}) ਦੇ ਅੰਦਾਜ਼ੇ ਲਈ ਇੱਕ ਸੋਧਿਆ ਤਰੀਕਾ ਕੈਪੇਸੀਟੈਂਸ–

ਵੋਲਟੇਜ ਮਾਪਾਂ ਦੀ ਵਰਤੋਂ ਕਰਦੇ ਹੋਏ ਇੱਕ ਘੋਲ–ਪ੍ਰੋਸੈਸਡ ਪਾਈਜ਼ੋਸੈਰਾਮਿਕ ਪਤਲੀ–ਫਿਲਮ MπM ਸਮਾਨਾਂਤਰ–ਪਲੇਟ ਕੈਪੇਸੀਟਰ ਬਣਤਰ ਦੀ ਵਿਸ਼ੇਸ਼ਤਾ ਲਈ ਵਿਕਸਤ ਕੀਤਾ ਗਿਆ ਹੈ। ਜਹਾਜ਼ ਤੋਂ ਬਾਹਰ ਲੰਮੀ ਲੰਬਾਈ ਅਤੇ ਟ੍ਰਾਂਸਵਰਸ ਲੰਬਾਈ ਨੂੰ ਉਤਸ਼ਾਹਿਤ ਕਰਨ ਲਈ ਕੈਪੀਸੀਟਰ 'ਤੇ ਇਲੈਕਟ੍ਰੀਕਲ ਲੋਡਿੰਗ ਲਾਗੂ ਕੀਤੀ ਗਈ ਸੀ। ਨਤੀਜਿਆਂ ਨੂੰ FEM–ਅਧਾਰਿਤ ਮਾਡਲਿੰਗ ਦੀ ਵਰਤੋਂ ਕਰਕੇ ਪ੍ਰਮਾਣਿਤ ਕੀਤਾ ਗਿਆ ਸੀ ਅਤੇ ਸਾਹਿਤ ਵਿੱਚ ਕਈ ਮਾਪਾਂ ਨਾਲ ਤੁਲਨਾ ਕੀਤੀ ਗਈ ਸੀ, ਜਿਸ ਵਿੱਚ ਪਾਈਜ਼ੋਰੇਸਪੌਂਸ ਫੋਰਸ ਮਾਈਕ੍ਰੋਸਕੋਪੀ–ਅਧਾਰਿਤ ਮਾਪ ਸ਼ਾਮਲ ਹਨ, ਜੋ ਆਮ ਤੌਰ 'ਤੇ ਟਿਪ–ਕੈਂਟੀਲੀਵਰ, ਅਤੇ ਚਾਰਜ ਕੀਤੇ ਨਮੂਨੇ ਦੀ ਸਤਹ ਦੇ ਵਿਚਕਾਰ ਮਜ਼ਬੂਤ ਇਲੈਕਟ੍ਰੋਸਟੈਟਿਕ ਪਰਸਪਰ ਪ੍ਰਭਾਵ ਕਾਰਨ ਭਰੋਸੇਯੋਗ ਨਹੀਂ ਮੰਨੇ ਜਾਂਦੇ ਹਨ, ਜਿਸ ਵਿੱਚ ਅਜਿਹੀਆਂ ਕਲਾਕ੍ਰਿਤੀਆਂ ਜਾਂਚ ਦੇ ਅਧੀਨ ਸਮੱਗਰੀ ਦੇ ਇਲੈਕਟ੍ਰੋਮੈਕਨੀਕਲ ਪ੍ਰਤੀਕ੍ਰਿਆ ਦੇ ਬਹੁਤ ਜ਼ਿਆਦਾ ਅੰਦਾਜ਼ੇ ਦਾ ਨਤੀਜਾ.

ਇਸ ਤੋਂ ਇਲਾਵਾ, ਇੱਕ ਮੈਟਲ–ਪੀਜ਼ੋ–ਮੈਟਲ (MπM) ਆਧਾਰਿਤ ਸਿੰਗਲ–ਪਿਕਸਲ (ਸੈਂਸਿੰਗ ਐਲੀਮੈਂਟ ਜਾਂ ਊਰਜਾ ਹਾਰਵੈਸਟਰ) 1x1 ਸੈਂਟੀਮੀਟਰ ਊਰਜਾ ਹਾਰਵੈਸਟਰ ਨੂੰ ਐਲੂਮੀਨੀਅਮ–ਕੋਟੇਡ ਪੋਲੀਥੀਲੀਨ ਟੇਰੇਫਥਲੇਟ (ਪੀਈਟੀ) 'ਤੇ ਹੱਲ–ਪ੍ਰੋਸੈਸਡ ਪੋਟਾਸ਼ੀਅਮ ਸੋਡੀਅਮ ਨਿਓਬੇਟ ਫਿਲਮਾਂ ਦੀ ਵਰਤੋਂ ਕਰਕੇ ਬਣਾਇਆ ਗਿਆ ਸੀ। ਸਬਸਟਰੇਟਸ ਫੁੱਲ–ਵੇਵ ਡਾਇਓਡ ਬ੍ਰਿਜ ਰੀਕਟੀਫਾਇਰ ਸਰਕਟ ਦੀ ਵਰਤੋਂ ਕਰਦੇ ਹੋਏ ਸ਼ੁਰੂਆਤੀ ਮਾਪ ਵੇਰੀਏਬਲ ਪ੍ਰੈਸ਼ਰ ਦੀ ਵਰਤੋਂ 'ਤੇ (~ 0.13 sec) ਦਾ ਅਸਲ–ਸਮੇਂ ਦਾ ਜਵਾਬ ਸਮਾਂ ਦਿਖਾਉਂਦੇ ਹਨ। ਪੈਦਾ ਹੋਏ ਵੋਲਟੇਜ ਸਿਗਨਲ ਦੀ ਤੀਬਰਤਾ ~ 40 mV ਅਤੇ ~ 1.4 V ਦੀ ਸੰਭਾਵਿਤ ਸੁਧਾਰੀ ਗਿਰਾਵਟ ਤੋਂ ਵੱਧ ਹੈ, ਜੋ ਹਾਰਵੈਸਟਰ ਵਿੱਚ ਮਹੱਤਵਪੂਰਨ ਚਾਰਜ ਟ੍ਰਾਂਸਡਕਸ਼ਨ ਦਾ ਸੁਝਾਅ ਦਿੰਦੀ ਹੈ।

ਸੰਖੇਪ ਵਿੱਚ, ਡਾਕਟੋਰਲ ਕੰਮ ਦੇ ਕੋਰਸ ਵਿੱਚ, ਸਮੱਗਰੀ ਵਿਕਾਸ, ਸਮੱਗਰੀ ਦੀ ਵਿਸ਼ੇਸ਼ਤਾ, ਡਿਵਾਈਸ ਡਿਜ਼ਾਈਨ, ਡਿਵਾਈਸ ਫੈਬਰੀਕੇਸ਼ਨ, ਅਤੇ ਚਰਿੱਤਰੀਕਰਨ ਜਿਸ ਵਿੱਚ ਹੱਲ–ਪ੍ਰੋਸੈਸਡ ਲੀਡ–ਮੁਕਤ ਸਮੱਗਰੀ ਸ਼ਾਮਲ ਹੈ, ਕੀਤੇ ਗਏ ਹਨ।

Contents

Acknowledgements **ii**

Abstract **v**

Contents **xi**

List of Figures **xv**

List of Tables **xxi**

1 Introduction **1**

1.1 Overview 1

1.2 Piezoelectric Effect 4

1.2.1 Brief History 4

1.2.2 Origin of Piezoelectricity 4

1.2.3 Electromechanical Coupling 5

1.3 Motivation 6

1.4 Scope 9

1.5 Choice of Material 10

1.6 Objectives 11

1.7 Thesis Organization 12

2 Methods and Material characterization **13**

2.1 Introduction 13

2.2 Thin Film Fabrication 14

2.3 Characterization Methods 15

2.3.1 Elemental Characterization Tools 15

2.3.2 Atomic Force Microscopy 15

2.3.3 COMSOL Simulation 16

2.4 Material Characterization 18

2.4.1 Calcinated Powder 18

2.4.2 Elemental Analysis 18

2.4.3 Thin Film Characterization 20

2.5 Piezo Response Force Microscopy 22

2.6 Thermal Budget 25

2.7 Summary 25

3 Thin Film Fabrication and Densification **27**

3.1 Introduction 27

3.2 Experimental Procedure 28

3.2.1 Device Fabrication 28

3.2.2 Characterization 31

3.2.3 Application of Electric Field 31

3.2.4 Volume Reduction Algorithm 31

3.3 Results and Discussion 33

3.3.1 Electric-Field Effect 33

3.3.2 COMSOL Simulations 33

3.3.3 Stoichiometric Analysis 34

3.3.4 Volume Reduction Calculation 38

3.3.5 Discussion 39

3.4 Summary 39

4 Extraction of Electromechanical Coefficient from CV Measurement **41**

4.1 Introduction 41

4.2 Experimental Section 42

4.2.1 Thin Film Fabrication 42

4.2.2 Device Fabrication 43

4.2.3 Capacitance vs Voltage Measurement 43
4.2.4 FEM Simulations 45
4.3 Theory 45
4.3.1 Piezoelectric Theory 46
4.3.2 $M\pi M$ based Analysis 47
4.4 Results 49
4.4.1 CV Analysis 49
4.4.2 Extracted d_{33} 51
4.5 Discussion 51
4.6 Summary 54

5 Energy harvesting device fabrication : an application **57**
5.1 Introduction 57
5.2 Experimental Section 58
5.2.1 Device Fabrication 58
5.2.2 Device Characterization 61
5.2.3 Test Setup 61
5.2.4 Device Simulation 63
5.3 Results and discussion 63
5.3.1 Morphology and Film Thickness 63
5.3.2 Flexion Testing 63
5.3.3 Device Stimulation 64
5.3.4 Time-Domain Output 65
5.3.5 Simulated Device 66
5.3.6 Charge Storage 67
5.3.7 Endurance Testing 68
5.3.8 Poling Effect 68
5.3.9 Comparison with P(VDF-TrFE) 69
5.4 Summary 69

6 Conclusions and Future Scope **71**

Additional work **74**

A Electrodeposited Silicon **77**

B PIN Diode **85**

C Solar Cell Fabrication **91**

D Supplementary Script **99**

E Publications **103**

F Biography **105**

List of Figures

1.1 Sales growth of major semiconductor product categories for year 2021-2026 [15]. Note: Total O-S-D is Opto, Sensor, and discrete. 3

1.2 Schematic representation of ABX_3 crystal structure. 5

1.3 Classification of crystal system point groups. 5

1.4 Schematic representation of direct and converse piezoelectric effect [24]. 6

1.5 Market share (2019-20) of sensor and actuator based technology. 7

1.6 Power requirement and energy harvesting ranges. 8

1.7 Schematic representation of a possible research cycle for development of new hybrid materials. 8

1.8 Market forecast for the growth of commercial piezoelectric device market [32]. 9

1.9 Commercially available piezoelectric technological classification based upon layer thickness [32]. 10

2.1 COMSOL workflow for the simulations. 17

2.2 Total surface displacement of PFM tip simulated using COMSOL. The PFM tip contains a flexible end and a stationary end bounded to replicate real time measurements. The applied bias of $-10\,\mathrm{V}$ was applied that resulted in the positive z-direction motion (pm) of tip represented by a color bar on the right. 17

2.3 (a) Schematic of PFM measurement, (b-d) XRD data of un-annealed and annealed (at 750 °C) KNN, (e) KNN unit cell. 19

2.4 XPS spectra for $K_xNa_{1-x}NbO_3$ layers with x=0.3, 0.5, and 0.7 respectively (the solid colored blocks are drawn as aid for the eye to elements of attention). 20

2.5 X-ray diffraction data ((a), (b), and (c)) for thin films of KNN (K:Na ratios = 30:70, 50:50 and 70:30). Substrate (W) peaks are indicated. Surface roughness (RMS) for these compositions are measured to be ~ 16.5 nm, 15 nm, and 48.3 nm, respectively, in the corresponding AFM scans ((d), (e), and (f)). 21

2.6 Raman spectra for $K_xNa_{1-x}NbO_3$ layers with x=0.3, 0.5, and 0.7 respectively (the solid colored lines are drawn as aid for the eye). 21

2.7 Amplitude and Phase vs excitation frequency of SPM cantilever near resonance and its voltage dependence response. Marked frequency of operation 35 kHz. 22

2.8 (a) Phase information for KNN (50:50) as a function of variable voltage, (b) Stoichiometry dependent piezo-response measurement by PFM for the KNN film with x = 0.3, 0.5, and 0.7 respectively at 8V drive amplitude. Inset: phase vs voltage hysteresis loop, (c) Measured FHA_D values at zero and maximum negative applied DC voltage, and coercive voltage for each composition. 24

2.9 PFM (Piezo-response force microscopy) and simulated response (black line with square symbols) for KNN (50:50) thin films. 24

3.1 (a) Image and schematic of fabricated lateral diode on SiO_2 substrate for implementing the process of electric field-induced annealing of inorganic (KNN) thin films for densification. Two different types of lateral designs were implemented (refer Fig. 3.2), (b) Atomic force microscopy data for the deposited KNN film (thickness ~ 4.5(2) μm, surface roughness ~ 6.8(2) nm). 28

3.2 (a) Schematic of the two geometries employed: type-A and type-B. The red dotted line represents the central symmetric axis across channel length. (b) The top view schematic (type-A and type-B) of the substrate chip with constant width (W=10 μm). Refer to Table (3.2) for actual dimensions (L1-L5). 30

3.3 Estimated crack regions: (a) Original layer, (b) Estimated background, (c) Result of the background-subtraction step, (d) Noise removed threshold image: a mask for the crack regions. 32

3.4 Estimating crack boundaries and manual labelling: (a) Detected edges, (b) Mask applied over the edges to estimate noiseless crack-boundaries(shown in green), (c) Contracted/cracked regions manually filled between the estimated boundaries (shown in white), (d) The estimated crack regions superposed over the original image (cracks in blue). 32

3.5 SEM image shows the before and after image of the processed film on Type-B substrate. . . . 33

3.6 (a.) Modeling design Type-A (pad size ∼ 100 μm). A bias of 30 V was applied that is represented by a color bar on the right (red is high potential and blue is ground). (b.) Electric field distribution on silicon wafer for design Type-A (pad size ∼ 100 μm). 34

3.7 2D heat map of lateral device geometry (a) Type-A and (b) Type-B showing temperature profiles (color bar represents the measure of intensity). (c) The calculated temperature profiles of Type-A and Type-B substrate geometries (across channel width and along contact pads) as predicted by the COMSOL simulations (inset: COMSOL temperature profile). (d) Channel temperature dependence on applied voltage for both the design geometries. 35

3.8 The post annealed cracked morphology with cracks resembling the electric field patterns predicted by the COMSOL simulations (inset). 35

3.9 (a) Schematic representation of the substrate with marked locations (P1 to P4) for EDX measurements (the represented dimensions are not to scale but for the purpose of understanding only), (b-e) SEM images (inset: EDX measurements location (yellow circle) and results) showing the stoichiometric shift in the composition of KNN from 51:49 to 31:69 post electric field exposure at different locations. SEM image sequence is (b) to (e) which represents locations (P1) to (P4) respectively (please refer Table (3.3)). 37

3.10 Calculation of area reduction due to densification. A region on the electrode was selected and a mask was obtained using background subtraction and global thresholding. The figure in the first row is the SEM scan performed on the post-processed KNN. The second figure shows the segmented cracks and the third figure shows the crack regions as red superimposed on the original image. 38

4.1 (a) KNN based thin film $M\pi M$ capacitor schematic and fabricated device image (where R_0 and h_0 are top electrode radius and KNN material thickness at zero DC bias, respectively), (b) A schematic depicting expansion and contraction of the device under DC bias(external electric field parallel versus anti-parallel against internal electric field). The actual device dimensions are $R_0 \sim$ mm and $h_0 \sim$ nm (where, $R_0 \gg h_0$). The schematic images are not to scale. 44

4.2 Schematic for the measurement of KNN-based thin film $M\pi M$ capacitors (shaded in light pink), using a semiconductor parameter analyzer (SPA). R_0 and h_0 are equilibrium top electrode radius and KNN material thickness, respectively (not to scale: R_0 ($\sim$ mm) $\gg h_0$ ($\sim$ nm)). The bottom images are the real fabricated device (top view). The right half of the schematic shows simulated displacements of the top surface for various device areas at 10 V constant bias. The displacement translates into an expansion of Δh for piezoceramic in the z-direction with the anchored bottom contact. Inset: Simulation image of PFM tip displacement compared to a large area electrode. 45

4.3 Measured capacitance $C_{m,k}$ as a function of fabricated device area at two biasing extremes (-10 V and 10 V). The inset provides a zoom-in $C_{m,k}$ at a specific area. The slope of the graph provides the intrinsic capacitance c_π, which further provides the parasitic capacitance C_{par} according to the Eq. (4.1). 46

4.4 Measured capacitance ($C_{m,k}$) and intrinsic specific capacitance (c_π) of KNN based thin film capacitor against frequency for various biases. In order to avoid noisy measurement, the frequency range of 100 kHz to 1000 kHz was selected. Inset: detail of measured capacitance ($C_{m,k}$) and intrinsic specific capacitance (c_π) (-10 V to +10 V, with a step of 1 V). 50

4.5 $C_{m,k}$ (open circles) and c_π (solid triangles) as a function of bias voltage dependence of measured capacitance and extracted intrinsic specific capacitance. 50

4.6 Measured capacitance ($C_{m,k}$) and extracted intrinsic specific capacitance (c_π) at 1 MHz, depicting the parallel and anti-parallel behavior of the fabricated device, and simulated data (black) for device area $\sim 4\,\text{mm}^2$ and thickness ~ 70 nm (where, $R_0 \gg h_0$). Intrinsic specific capacitance (c_π) was extracted (Eq. (4.9)) for applied voltages of -10 V to +10 V. 51

4.7 Extracted Δh and d_{33} as a function of applied poling voltage. The equivalent poling field is shown on top x-axis for reference. 52

4.8 Extracted (Eq. (4.10)) and calculated (Eq. (4.9))[152] d_{33} as a function of frequency. Measured dielectric constant (κ_r) and dielectric loss ($tan\delta$) are shown on the right y-axis. 52

5.2 Fabricated device using $K_xNa_{1-x}NbO_3$ layer sandwiched between metal contacts and encapsulated in PDMS. 60

5.1 Schematic showing steps for substrate fabrication and device assembly. 61

5.3 Schematic of device characterization. The encapsulated device was mounted on a soft surface to enable easy bending in response to the impact by the shaker. The shaker head and the device were devised to be in contact at all times during the excitation at low frequencies. 62
5.4 Testing setup for stimulating PDMS encapsulated device. 62
5.5 Morphological scan of the deposited KNN layer with $\sim 4.5\,\mu$m layer thickness and ~ 16.8 nm surface roughness. 63
5.6 Flexibility testing of the device with and without PDMS encapsulation. 64
5.7 Testing setup for stimulating PDMS encapsulated device with finger pressing. 64
5.8 Generated output with finger pressing (see Video). 65
5.9 Un-rectified and rectified response of the device at 10Hz input. 65
5.10 Un-rectified and rectified output of the device at different input frequencies for a period of 5 sec (blue), and the maximum voltage obtained at respective frequency of operation (red). . . 66
5.11 Harvested (experimental, highlighted by light red) vs simulated (blue dotted lines have been added as an aid to the eye) device as a function of input excitation frequencies for different load transfer efficiencies of PDMS (Ω = 20 % to 100 %). The shaded area represents the agreement between experimental and simulated data about the range of load transferred (Ω = 60 % to 80 %). 67
5.13 Endurance testing of the DUT for ~25 minutes of operation with 5 Hz strike frequency. 68
5.12 Charging of capacitor (22 μF) indicating continuous conversion of applied force into energy. . 68
5.14 Unpoled vs poled KNN device layer response with 5 Hz strike frequency. 69

6.1 Schematic of future device design. 73

A.1 Schematic of electrodeposition of silicon. 78
A.2 Constant current (20 mA) profile of the electrodeposition. 79
A.3 Constant voltage (10 V) profile of the electrodeposition. 80
A.4 EDX elemental map of deposited Si layer. 81
A.5 EDX elemental distribution of deposited Si layer. 81
A.6 SEM image of deposited Si layer 82
A.7 XRD data for deposited Si layer. 82
A.8 Raman spectra of deposited Si layer. 83

B.1 PIN diode fabrication process flow. 87

B.2 Schematic of fabricated device (top and side view) with stack dimensions. 88
B.3 IV characteristic of the fabricated device and inset is a schematic of final device with thickness, layer resistance, and atom density. 88
B.4 PIN diode IV characteristic under illumination and dark. 89

C.1 Polysilane and polysiloxane molecules synthesized by Shankar et al.[249, 250] 92
C.2 Molecular species considered so far and their SSAO 94
C.2 Molecular structures of the species considered so far, and their spectral integration respectively. 95
C.3 SEM images. 96
C.4 Surface profile 96
C.5 Fabricated device 97
C.6 Current vs voltage characteristic of fabricated device under AM1.5G. 98

D.1 Algorithm flowchart. 99

List of Tables

1.1 Comparison between ICs systems and MEMS [7]. 2

2.1 Comparison of metal properties [66] for selection of cost effective and hardest metal for utilization as bottom electrode for PFM measurement. 15

2.2 KNN material properties [71, 72, 73, 74] used for modeling and simulation in COMSOL. . . . 18

2.3 Stoichiometric composition of as deposited ($K_xNa_{1-x}NbO_3$ or KNN) layers with x=0.3, 0.5 and 0.7, respectively. 'A' denotes total A-site occupation (A=K+Na). Errors in EDX data are estimated to be $\sim 2\%$ (based on bulk samples for this tool). 19

2.4 Comparison of elctro-mechanical coefficients using various deposition and characterization techniques. To capture the full thermal impact of the processes, we have estimated the thermal budget[83] of each report using the expression, $\Sigma_{k=1}^{k=N}\Delta t_k T_k$, where for an N step process, the time of each step (Δt_k) and the temperature of that step (T_k) is accounted in this figure of merit. LSV=Laser Scanning Vibrometry. BC=Berlincourt method. 26

3.1 Comparison of metal properties for selection of metal for utilization as bottom electrode in densification. The electrical (σ) and thermal (K) conductivities listed are at 275 K [110, 111]. . 29

3.2 Dimensions of devices with constant width (W=10 μm), variable channel lengths (L1 to L5), overlap active area, and volume. 30

3.3 Stoichiometric composition of ($K_xNa_{1-x}NbO_3$ or KNN sol) with x=0.5. 'A' denotes total A-site occupation (A=K+Na). The measurements were carried out on stock solution (standard: [K/A]:0.510, [Na/A]:0.489, [Nb/A]:0.937), and at different locations (P1 to P4, refer Fig. (3.9(a))) on the device after electric field exposure. Errors in EDX data are estimated to be $\sim 2\%$ (based on bulk samples for the tool). 36

4.1 Calculated d_{33} using the derived equation (Eq. 4.10) compared with the d_{33} from literature using different techniques: BC=BerlinCourt, PFM=Piezoresponse Force Microscopy, LDV=Laser Doppler Vibrometry, and CV=Capacitance-Voltage for estimation of electromechanical coefficient (d_{33}). The comparison contains our previous work on the estimation of FHA_d using PFM on KNN thin-films [71], and present work, correspond to thermally unannealed samples, while most other studies are for annealed samples. Owing to the use of inverse piezoelectric effect to determine d_{33} in our work, our measurements may be an underestimate by as much as 10-15% [147]. 55

5.1 Comparison of metal properties for selection of cost effective, soft, and flexible metal for utilization as soft conductive electrode (SCE) in flexible energy harvester device. 60

5.2 Performance comparison of flexible energy harvester based on KNN and P(VDF-TrFE) or composites. 69

C.1 SSAO comparison 95

C.2 Extracted parameters of the fabricated solar cell 98

Chapter 1

Introduction

1.1 Overview

Sensors, actuators, transducers in microelectromechanical systems (MEMS), and technologies using micro-optical devices such as atomic force microscopes (AFM), infrared (IR) detector arrays etc., connects the mechanical changes with changes in the charge state of the active piezoelectric layer of the device [1]. This interchange of energy state from mechanical to electrical or vice versa enables the implementation of sensors and transducers for various applications. Compared to other electromechanical transduction based technologies (Electro-Magnetic Induction etc.) piezoactive materials have high chemical and environmental stability can operate at high temperatures and possess high pressure per density for application in actuation devices. Apart from this, there are plenty of ways in which commercial devices dissipate/waste energy, which in principle, can be harvested for powering other electronics devices. This can be achieved by the implementation of functional piezoelectric ceramics for scavenging freely available vibrational energy in the environment. For ubiquitous deployment of MEMS-based vibration energy harvesters in distributed flexible sensors, fabrication processes must be cost-effective and environmentally friendly. Lead zirconium titanate (PZT) and other lead-based materials such as lanthanum-doped PZT (PLZT), $Pb(Mg_{1/3}Nb_{2/3})O_3$ $PbTiO_3$ (PMN-PT) dominate the market for piezoelectric materials due to their excellent electromechanical properties [2]. However, the presence of lead (60 % by weight) in these materials presents an environmental and health challenge that limits the regulatory approval for several classes of devices. Amongst several classes of piezo materials, lead-based ferroelectrics, PZT has been widely studied [3]. With a high Curie temperature (T_c >400 °C), and a high electromechanical coefficient (d_{33}=300 pC/N to 400 pC/N) for sputtered layers of sodium-potassium niobate ($K_xNa_{1-x}(NbO_3)$, (KNN)) based systems have received considerable attention as promising alternatives to PZT ceramics [4, 5,

6].

One of the major concerns for MEMS devices' reliability and operational performance is the residual stress generated in thin films during fabrication. The transduction mechanism for both sensors and actuators depends on the clamped or free-standing thin film for conversion of mechanical signal (vibration or stimulus) to an electrical signal or vice versa. Other problems associated with the use of piezoelectric thin films are the ageing of the material, polarization fatigue, frequency and field dependence of material for transduction originate from the domain wall displacement and is considered as an extrinsic property (dependent upon parameters such as thickness, poling, and growth orientation etc.) the treatment of which is challenging. The requirement of encapsulation is another layer of technical complexity that has been an active area of research, where a trade-off between the transfer of energy and extended shelf life takes place. Sensors and actuators failures are distinctive compared to standard digital IC's, and thus, their testing environment and technologies are also different [7]. These testing environments and modules have been designed with application specifications and are listed in Table. (1.1).

Table 1.1: Comparison between ICs systems and MEMS [7].

Testing approach	Integrated digital devices	Analog mixed signal devices	Microelectromechanical systems
Fault model	Assertion, gate delay, line delay, redundant, path delay, behavioral, branch, bus, cross-point, stuck-open, stuck-at, stuck-on, bridging, and so forth.	Hierarchical, behavioral, macro model, transistor, physical, catastrophic, and parametric faults and so forth.	Behavioral, shorts and opens in electrothermal and electromagnetic, structural defect level, parametric, functional, fatigue, and reliability model.
Test technique	VHDL, HSPICE, fault dictionary, probabilistic, signature analysis method, LFSR (linear feedback shift register), BIST (built in self-test), and so forth.	Pole-Zero Analysis, artificial neural network, HSPICE, SABER, VHDL-AMS, ATPG, diagnosis of soft faults based on fractional correlation, BIST (built in self-test), and so forth.	Neural network, VHDL-AMS, device-level (FEM) and HDLs and transposition of techniques developed for microelectronics, BIST (built in self-test).

In industry, the most growth is projected for sensors and actuators for the coming years, as shown in the Figure .(1.1). The manufacturing of piezoelectric-based MEMS has benefitted from infrastructure and technology developments in CMOS IC, and ferroelectric memories [8, 9]. The development of piezo active thin films is essential to realize highly integrated MEMS devices; for example, the growth of textured, high-quality polycrystalline perovskite thin films and complex chemistry has become routine. The integration of piezoelectric materials (PZT, KNN, PVDF etc.) with MEMS and NEMS require the film thickness to be in micro to the nanoscale, where the behavior of the material is different when compared to bulk properties [10]. Current industrial technology nodes are below 10 nm, and at such small length scales, the properties and behavior of materials change drastically (a typical example is monolayer carbon known as graphene). Piezoelectric thin

films are highly prone to defects induced/introduced during processing which alters the performance of the fabricated device, which includes stoichiometric variation due to the volatile nature of the compounds involved, microstructural heterogeneities, mechanical stress at domain boundaries, and introduction of impurities [10, 11, 12]. Although other effects such as electrode interface, grain boundary, and surface interactions can be rectified by tailored chemistry, alternate metals, and heat treatment to a certain point where the grain size is more significant than domain size [13]. It has been demonstrated both experimentally and theoretically that domain wall mobilities and domain densities have vast effects of film thickness [14].

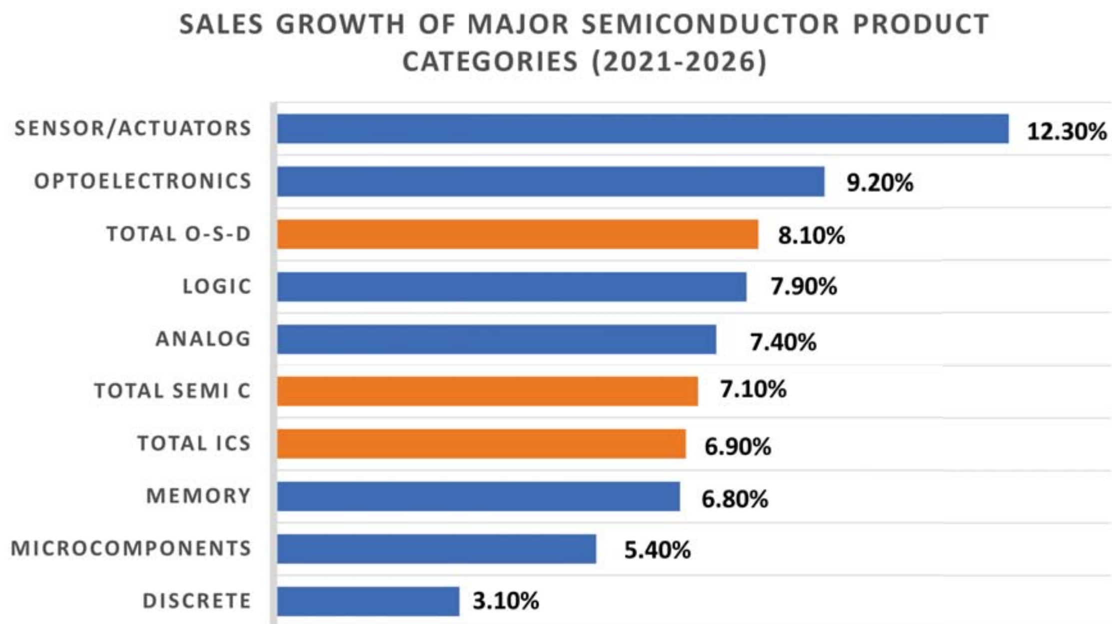

Figure 1.1: Sales growth of major semiconductor product categories for year 2021-2026 [15]. Note: Total O-S-D is Opto, Sensor, and discrete.

The benefits, on the other hand, for integration of piezo active thin films is that the deposition conditions in CVD, PVD, LPCVD, sol-gel synthesis etc. can be highly tailored and controlled to create metastable phase, which is generally difficult to achieve by quenching in bulk material [16, 17]. This also provides an opportunity to grow a multilayered stacked device structure with controlled film orientations. The classical approach for integrating two different kinds of processes comprise of trade-off features such as flexibility, performance, or ease of fabrication of standard device structures such as processing back side micromachining the final steps of a standard MEMS cantilever based energy harvester as the last step using a high-end instrument such as a DRIE (direct-reactive ion etching) without compromising or damaging the on-chip pattern or layers. The CMOS fabrication process involves wetting patterned IC's or wafers in different solvents and de-ionized water several times, which should not affect the thin film or create stress resulting in failure or damage.

1.2 Piezoelectric Effect

1.2.1 Brief History

In 1880, the Curie brothers discovered the capability of certain crystals (quartz, Rochelle salt, topaz, and tourmaline) to generate an electric charge in response to mechanical stress or simply pressing/squeezing [18]. The phenomenon is termed ‘piezoelectric effect’, where ‘piezo’ means ‘push’ in Greek. Another unique property about this effect was its reversibility. In other words, the converse piezoelectric effect, which mathematician Gabriel Lippman demonstrated in 1881, where applied electric field resulted in deformation due to mechanical stress [19]. The piezoelectric effect arises from the non-centrosymmetric central atom in a crystal structure (Fig. (1.2)) of certain materials (e.g. quartz) that causes unequal charge distribution in a single unit. In normal conditions, the dipole moment vectors arising due to the unequal charge distribution cancels each other out. However, under deformation or mechanical stress, a resultant net negative and a net positive charge gets created on each face of the unit cell [20]. Due to the underdeveloped theory and complex mathematics involved, the discovery of piezoelectric materials remained in the laboratories for almost 30 years till the first world war broke [21]. During this period, the first application of such material was ultrasonic submarine detection using quartz crystal [22]. Thus, from 1917 till today, this reciprocity relation between electrical-mechanical loading in piezo-active materials due to the piezoelectric effect has been exploited for applications in sensors, actuators, telecommunications, and medical diagnostics.

1.2.2 Origin of Piezoelectricity

Non-centrosymmetry is considered to be the main requirement for the origin of piezoelectricity in different materials systems, for example, aluminium nitride (AlN), quartz, and lead zirconium titanate (PZT), which results in a spontaneous polarization due to separation of charge distribution/centres [23]. Perovskite material system (ABX_3, (Fig. (1.2))) discovered in 1830 by Geologist Gustav Rose, and named after Russian Mineralogist, C. L. A. Von Perovski, is the most common material structure that exhibits spontaneous polarization. In the perovskite structure, A and B are metallic cations. In contrast, X is a non-metallic anion species (generally oxygen or halide), making a primitive cubic system with Pm3m symmetry with $r_A \gg r_B$ (where, r = atomic radius), shown in Fig. (1.2).

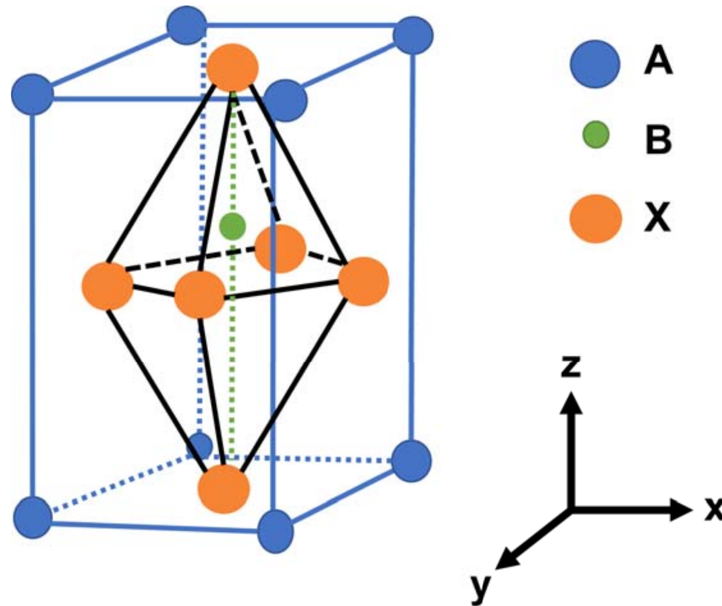

Figure 1.2: Schematic representation of ABX_3 crystal structure.

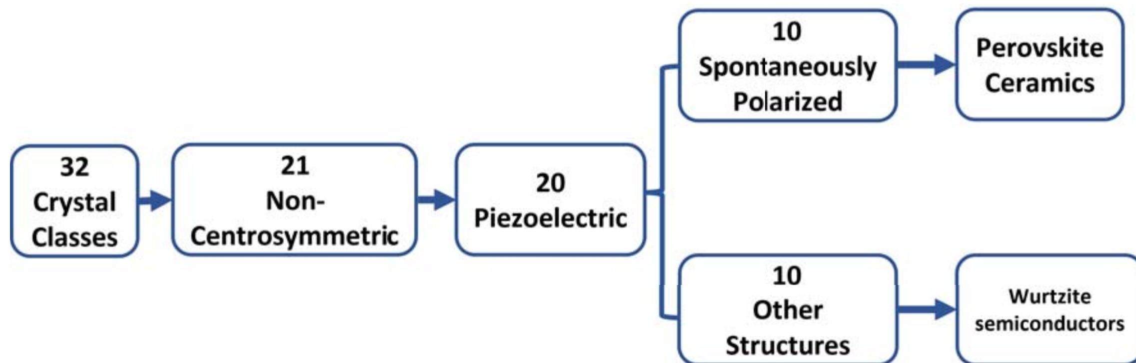

Figure 1.3: Classification of crystal system point groups.

Structural Origin

The observation made by the Curie brothers about the generation of electricity under mechanical pressure was for certain crystals, including topaz, quartz, Rochelle salt, and cane sugar, was enough to anticipate that crystal symmetry plays a decisive role in the origin of the piezoelectric effect. The piezoelectric effect is attributed to the spontaneous polarization that originates due to the structure of the crystal. Out of 32 crystal classes (or point groups), 21 posses non-centrosymmetry but only 20 are classified as piezoelectric (Fig. (1.3)).

1.2.3 Electromechanical Coupling

A piezoelectric material's ability to develop potential (V) which is directly proportional to the applied stress (i.e. change in thickness) as shown in Fig. (1.4) is a reversible property (as shown in Fig. (1.4)) where an applied potential can generate electric displacement [24]. This reversibility property has classified the piezoelectric

effect as a direct and converse piezoelectric effect, and based upon this fundamental property, the material can be used in applications such as sensing or actuation.

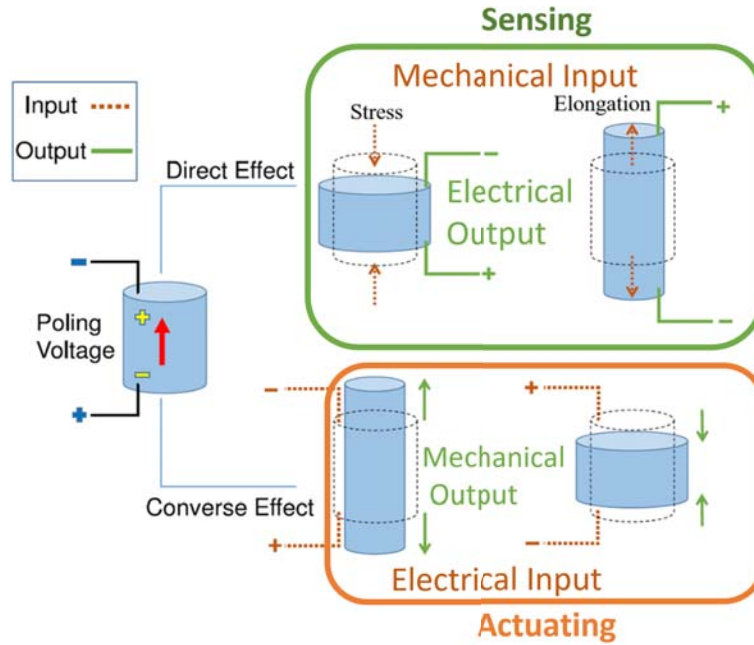

Figure 1.4: Schematic representation of direct and converse piezoelectric effect [24].

The fundamental piezoelectric constitutive relations (Eqs. (1.1)), can predict the change in device geometry under a given bias. Using the strain-charge form, one can represent the interactions between mechanical stress (σ), mechanical strain (ϵ), electric field (E), and electric displacement (D) within a material [25] in the following form:

$$\begin{aligned} \mathbf{D} &= d\boldsymbol{\sigma} + (1+\chi_e)\mathbf{E} \\ \boldsymbol{\epsilon} &= \frac{1}{Y}\boldsymbol{\sigma} + d^T\mathbf{E} \end{aligned} \tag{1.1}$$

, where d is the piezoelectric tensor, and χ_e is the electrical polarizability of the dielectric, and Y is Young's modulus.

1.3 Motivation

Environment and energy are the two most critical issues humanity and the planet faces in the modern world. All kinds of commercially available technologies (sensor/actuator) have distinct stimulus mechanisms of op-

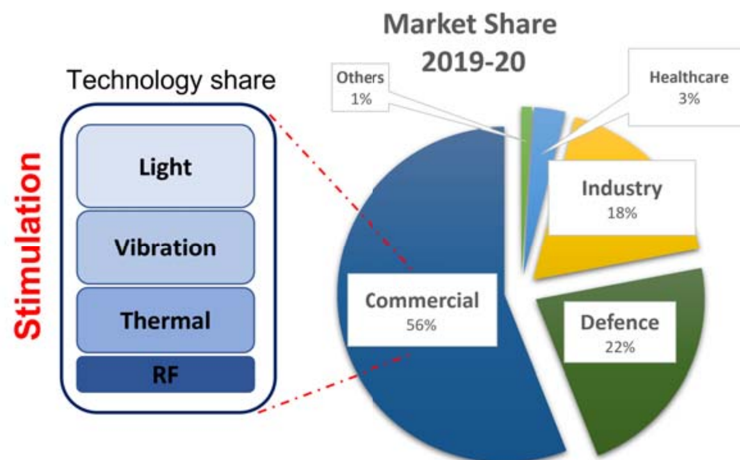

Figure 1.5: Market share (2019-20) of sensor and actuator based technology.

eration, where light and vibration-based stimulation techniques dominate (Fig. (1.5)) the device market due to abundance in the environment. Another reason for such dominance is the ease of integrating light and piezo active materials into existing CMOS fabrication processes and their small form factor (area/volume required for activation function).

The consumer landscape is going through digital transformation, where batteries are the most crucial device component, costing huge real estate on the device. The batteries also contain heavy metals like lead, mercury, and lithium, which are not environmental friendly both in mining or in the decomposition process. Technical advancements like shrinking the device's size, better algorithms to run devices, idling devices when not in use can prevent battery drain but are not the permanent solutions to the problems because batteries have a limited lifespan. Although there is a drastic decrease in the power requirement of the electronics components and an increase in the autonomous status of devices that do not depend upon conventional energy sources or storage techniques such as batteries (Fig. (1.6)) [26]. Lead-based solid solutions dominate the piezo-based energy harvesters, actuators, and sensors due to their competitive properties such as high electromechanical coefficient and minor effect of temperature change due to the presence of stable morphotropic phase boundary [27]. The environmental concern arises from the high concentration of lead present in the devices and the related effects that arise from the pre-production and post-disposal of these devices [28]. Thus, the regulation of hazardous substances (RoHS) established by the European Union had imposed strict regulations on the use of lead in electronics devices, which, in turn, prioritized the development of lead-free piezoceramic with comparable piezoelectric properties that can compete and replace the lead-based devices in the market [29]. Lead-free piezo-electrics have achieved enormous progress under these circumstances, for example, (Bi0.5Na0.5)TiO3-BaTiO3 (BNT-BT) based, BaTiO3 (BT) based, BiFeO3 (BFO) based, and (K, Na)NbO3

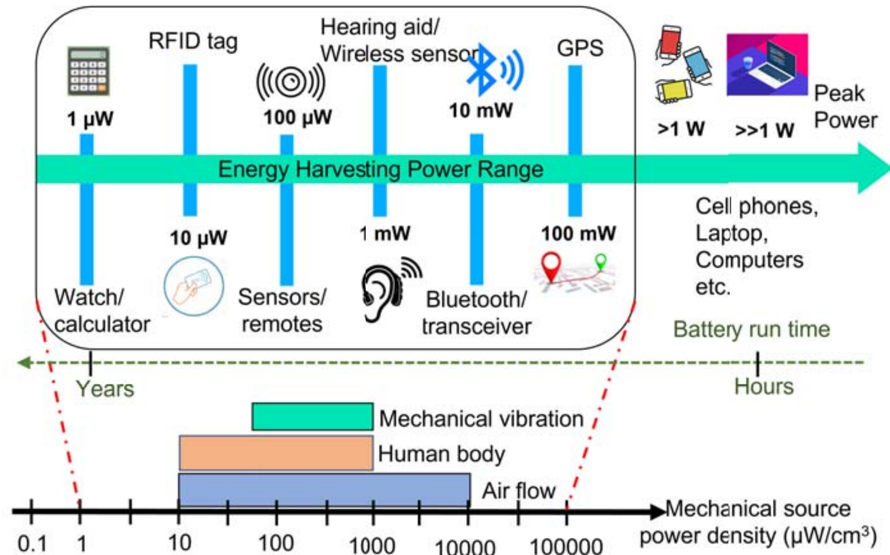

Figure 1.6: Power requirement and energy harvesting ranges.

(KNN) based piezoceramic systems are under exploration extensively [30].

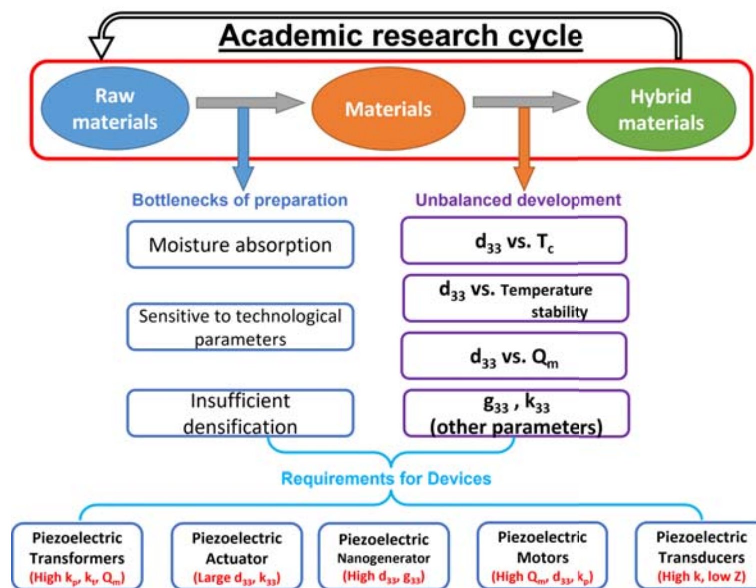

Figure 1.7: Schematic representation of a possible research cycle for development of new hybrid materials.

Although there has been enormous progress in the field of piezoelectric material research in academia, academic research only contributes towards basic research of the material. The academic research cycle, as shown in Fig. (1.7), only focuses on the development of material (raw to hybrid). The focal point of academic research is publication. The target is always increment of some figure of merit parameter such as temperature stability, high performance etc., which translates into unbalanced development. The researchers neglect the bottlenecks of the process called; 'from lab to product' and shift their focus from material properties required for application standpoint to only material properties. Thus, the development of the material synthesis process

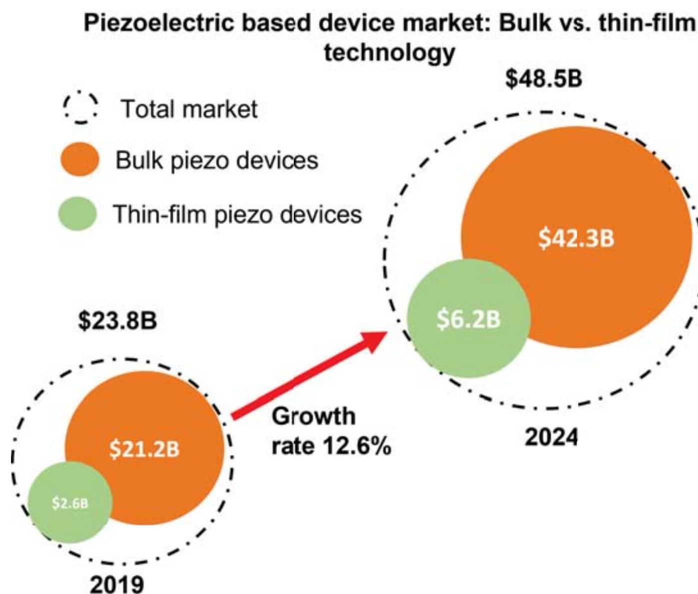

Figure 1.8: Market forecast for the growth of commercial piezoelectric device market [32].

to device fabrication was the motivation for this thesis.

1.4 Scope

Piezoelectric devices have become a key component for many industrial, defense, aerospace, and consumer-based products. The growth rate of the piezoelectric device market has experienced a robust lift from USD 21 billion in 2015 to USD 30 billion in 2020 and can rise to USD 42.3 billion by 2024 with a 12.6 % growth rate (Fig. (1.8)) [31, 32]. During this forecast period, the piezoelectric polymers will have the highest growth rates amongst the group of available piezoelectric materials due to the unique features such as lightweight, easy processing, low fabrication cost, environment friendly, and bio-compatibility [33]. These materials are bio-implantable, non-reactive, super sensitive, and most importantly, compliant with regulations of the restriction of hazardous substances (RoHS) [29, 28]. The main aim of the present work is to explore a low-cost, non-toxic, high output, flexible, and biocompatible piezoelectric material. In the current electronic device market, there are two deposition techniques that are competing head-on, i.e. PVD and Sol-Gel. Advantages of PVD are its uniformity, consistency, and already existing infrastructure in the fab industry (supply chain), whereas Sol-Gel provides better intrinsic film, better control over stoichiometry, high uniformity, easy process modification, and potential of printing techniques. Thus, sol-gel processed perovskite potassium sodium niobate ($K_xNa_{1-x}(NbO_3)$ KNN) seems like a plausible material candidate for applications in flexible electronics such as energy harvesting or tactile sensor.

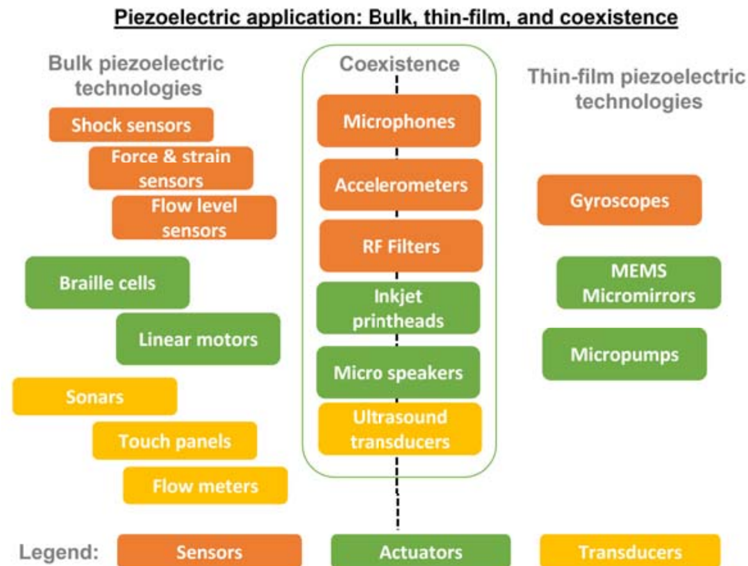

Figure 1.9: Commercially available piezoelectric technological classification based upon layer thickness [32].

Conventional piezo devices were fabricated as a single piece or bulk ceramic to be integrated with products ranging from low-tech (e.g. gas lighter) to high-tech (ultrasound probes). Advanced piezo materials in the form of thin-films have been developed in the past couple of decades, where piezoelectric thin films have been integrated with semiconductor fabrication processes in order to accommodate the demand of ever-decreasing size (miniaturization) and increasing functionality of electronic devices in the modern-day. Thus, thin-film piezoelectric deposition techniques are gaining interest in the industry and academia, where different material systems are being developed based upon not only functionality but also deposition techniques. Although transitioning from bulk to thin-film piezoactive materials have been achieved for several devices due to miniaturization, special application based use-case devices still exist in the market as shown in Fig. (1.9) for example, ultrasound detectors for medical applications. It is also evident from the market survey that the miniaturized micromachined thin-film devices such as gesture, face, and fingerprint recognition systems are a new norm of the modern world. Ultrathin speakers are another thin-film piezoactive material based market demonstrating up to 0.45 mm thickness speakers.

1.5 Choice of Material

Amongst all the candidates to replace lead-based ceramics, KNN has been an excellent choice that has demonstrated equivalent d33 comparable to PZT [34]. Technological interest in the perovskite potassium sodium niobate ($K_xNa_{1-x}(NbO_3)$ KNN) [35, 36] has grown over the previous decade due to the high electromechanical coefficients observed in bulk [37], sputtered [38], ball-milled [36], electrophoretic [39], 1D/2D materials [40],

and sol-gel deposited films [41]. In comparison, reasonable control over stoichiometry arose from heat treatment of the material to gain dense and sintered films. Limited thickness of KNN-based films and relatively high sintering temperature make the volatilization of alkali elements inevitable [42]. During sol-gel synthesis, it is often observed that the synthetic products are Na-rich compared to the precursor chemistry [42]. This has implications for phase boundaries and poling conditions needed for piezoelectric KNN. On the other hand, given the greater covalent radius of potassium (2 Å) compared to sodium (1.6 Å), it is possible that imposition of crystal deformation in a K-rich material compared to the standard orthorhombic structure of KNN (50 % K-composition), may result in interesting electromechanical properties. The properties of sol-gel deposited KNN film with a significant excess of the K-precursor, resulting in $K_{70}Na_{30}(NbO_3)$, in contrast to the commonly studied $K_{50}Na_{50}(NbO_3)$ composition has been studied. Process development[43] of KNN involving thin (~ 70nm) films is expected to provide an alternative process pathway to production of devices such as energy harvesters[44] for autonomous sensors[45], and transducers[26, 46]. In literature, it has been consistently noted that sputtering under vacuum can produce orthorhombic phase[38] of KNN for compositions approaching K:Na=1:1 (x=0.5), which produces the highest observed d_{33} parameter [47]. As a complicating processing step, annealing of KNN films, which is commonly used for densification of films, involves the use of high temperatures for favorable crystal structures to increase piezoresponse, is also known to produce changes in the designed K:Na ratios[42].

In amorphous, or nanocrystalline materials synthesized in solution phase, we expect the material to exhibit very short range order composed of a mixture of phases - cubic (C), tetragonal (T) and orthorhombic(O) [41]. As a result, the performance of sol-gel deposited KNN thin films has been expected to be relatively poor[48]. However, under application of intense electric fields comparable to published poling parameters[49, 50] at nanoscale, it is perhaps possible to locally induce highly ordered crystal structures with corresponding electromechanical performance. Further, the greater expectation of strain in K-rich KNN compositions is expected to enhance the freedom of motion of the central Nb in the crystal structure[51, 52].

1.6 Objectives

The objective of this work was to study sol-gel processed perovskite potassium sodium niobate ($K_xNa_{1-x}(NbO_3)$ KNN) for its application in flexible electronics such as energy harvesting or tactile sensor.

The Focus was on the following aspects:

1. Investigate the influence of stoichiometric fluctuation on the electromechanical properties of KNN ce-

ramic.

2. Use of simple and inexpensive techniques for layer deposition.
3. Optimization and characterization of the thin film.
4. Development of a new low-cost densification method.
5. Development of a lateral technique for characterization of piezoelectric coefficient of the material.
6. Application of thin films for energy harvesting device fabrication.
7. Assessment of fabricated energy harvester.

1.7 Thesis Organization

The present thesis is a compilation of work done for the award of PhD and consists of seven chapters, the first being the introduction. The first chapter consists of the introduction to the field, brief history of piezoelectricity, some useful definitions of the field for the unfamiliar individual or experts/specialists of other fields. The introduction provides useful information for the understanding of the work described in this thesis and discusses some potential material candidates based upon their advantages. The second chapter begins with the overview and development of the synthesis process and the material characterization process of the selected material. The third chapter consists of thin-film fabrication and optimization. It also investigates the complications that arise during the densification process. The fourth chapter explores the possibility of extraction of electromechanical coefficient via a simple capacitor structure fabrication to develop an auxiliary process alternative to piezoresponse force microscopy. The fifth chapter serves as an implementation of the hypothesis presented here and illustrates a working device fabrication and its characterization as an energy harvesting device. The sixth chapter concludes the thesis and reviews some future aspects and potentials of the current work, which may help in the advancement of further knowledge in the field. The final chapter highlights some additional experimental assignments completed as a parallel endeavour during the present work.

Chapter 2

Methods and Material characterization

2.1 Introduction

Technological interest in the perovskite potassium sodium niobate ($K_xNa_{1-x}(NbO_3)$ KNN) [5, 6] has grown over the previous decade due to its low toxicity, biocompatibility, and high electromechanical coefficients [5] observed in hydrothermal [53], sputtered [54], ball milled [6], electrophoretic [55], 1D/2D materials, [40] and sol-gel deposited films [56]. The performance of KNN compares favorably with the performance of industrially relevant, but environmentally deprecated materials composed of lead perovskites like PZT, PMN-PT, etc. [5]. Process development [43] of KNN involving thin (~ 70nm) films is expected to provide an alternative process pathway to production of devices such as energy harvesters for autonomous sensors, and transducers [5], interestingly for CMOS-compatible devices [1]. In literature, it has been consistently noted that sputtering under vacuum can produce orthorhombic phase [38] of KNN for compositions approaching K:Na = 1:1 (x=0.5), which produces the highest observed electromechanical coefficient [56]. As a complicating processing step, annealing of KNN films, which is commonly used for densification of films involves the use of high temperatures for favorable crystal structures to increase piezo response, is also known to produce changes in the designed K:Na ratios [56] altering the final stoichiometry of the film.

In solution-phase synthesis of amorphous, or nanocrystalline materials, we expect the material to exhibit very short range order composed of either amorphous material, or a mixture of phases - cubic (C), tetragonal (T) and orthorhombic(O) [57], resulting in relatively poor performance of sol-gel deposited KNN thin films [48]. However, under application of intense electric fields comparable to published poling parameters [58] at nanoscale, it is perhaps possible to locally induce highly ordered crystal structures with correspondingly superior electromechanical performance. Further, strain in K-rich KNN compositions is expected to enhance

the freedom of motion of the central Nb in the crystal structure [59]. Therefore, sol-gel based synthesis technique was chosen based upon the advantages such as stoichiometric control, soft synthesis processing, and high control over processing. In this chapter, we report the synthesis, deposition process, localized poling and measurement of electromechanical response of amorphous thin films of KNN ($K_xNa_{1-x}(NbO_3)$) with three different chemical compositions i.e. x=30, 50, and 70, respectively.

2.2 Thin Film Fabrication

Silicon substrates (University Wafers) were cleaned successively in an ion-free detergent (Alconox® Z273228, sourced from Sigma-Aldrich), deionized (DI) water, acetone, and 2-propanol before being exposed to ozone plasma (Novascan) before a 50 nm tungsten sputter step under 20 mTorr (Angstrom Engineering). Tungsten was used instead of the usual platinum to reduce the overall cost of the process. Piezoresponse force microscopy has evolved as a powerful technique to characterize ferroelectric materials at nanoscale which exploits the converse piezoelectric effect and detects the induced dynamic electromechanical response of the material when excited by the application of an ac voltage (V_{ac}) between the sample and the AFM cantilever tip (in contact mode acting as the top electrode) [60]. However, to probe the intrinsic ferroelectric nature of the material free from the artefacts such as substrate coupling or local mechanical clamping is still a challenge [61]. The non-ferroelectric contributions by the substrate and the conductive thin film can be reduced by carefully choosing the bottom electrode [62]. The properties that mostly affects the electrode selection for the electromechanical coefficient measurement (i.e. Tip/material/bottom electrode stack) are listed in Table. (2.1). Ti/Pt (Titanium/Platinum) is preferred over Cr/Au (Chromium/Gold) as the bottom electrode for PFM measurements due to its hardness and because the cantilever tip is also Pt coated. A Pt coated PFM tip creates a thin layer of PtO_x which stores charge by the applied voltage [63] which also replicate as a barrier layer between the bottom electrode (Pt) and the ferroelectric material [64]. This dielectric layer introduces secondary effects due to the changed overall dielectric constant, such as penetration depth of electric field and thus affects the field distribution inducing non-linear artefacts in the measurements [65]. Other parameters such as Young's modulus, coefficient of thermal expansion, and cost were also considered in selection of the bottom electrode for PFM measurements. The best candidate amongst the listed metals is tungsten due to its hardness, elastic modulus, and low coefficient of thermal expansion and market price.

The resulting substrates were cleaned again using the procedure above before being spin-coated (NXG-P2, APEX IC) with the KNN sol at 3000 rpm for 30 seconds, and annealed at 90 °C for 10 minutes for residual

Table 2.1: Comparison of metal properties [66] for selection of cost effective and hardest metal for utilization as bottom electrode for PFM measurement.

Metal	Density ρ (kg/m^3)	Hardness/UTS* σ (MPa)	Elastic moduli E (GPa)	Coefficient of Thermal Expansion ($\times 10^{-6}$ K^{-1})	Market Price** ($/kg)
Al	2710	120-180	70	23.5	3.3
Au	19300	188-216	79	14.1	57,967
Pt	21040	400-549	164	9.00	33,050
Ti	4540	500-620	118	8.60	18.0
W	**19400**	**3430-4600**	**410**	**4.5**	**35.3**

*UTS is Ultimate tensile strength.
**Market price collected form London metal exchange (Feb 2022) and Sigma-Aldrich (Feb 2022).

removal. Sol-gel route [43, 67] using acetate salts was employed to synthesize $K_xNa_{1-x}NbO_3$ (KNN) at three different compositions (x = 30, 50, and 70 mol%). The solution wetted the substrates well which resulted in dense thin uniform films with good adhesion to the substrate without any delamination or precipitation of the alkaline salts. The resulting films were measured (Table. 2.3) using a profiler (Alfa Step IQ, KLA-Tencor), that resulted in consistent ~ 68(2) nm thin films of the KNN.

2.3 Characterization Methods

2.3.1 Elemental Characterization Tools

X-ray diffraction (XRD) (PANalytical Xpert Pro) measurements in the Bragg-Brentano geometry and with Cu Kα (1.5418 Å) radiation with an Ni filter, were carried out with a step size of 0.02 °C and a scan rate of 0.5 °C/min. Energy-dispersive X-ray spectroscopy scans (EDX) and elemental ratios were collected from the as-synthesized thin films using Zeiss EVO SEM 50. Raman spectroscopy data (Horiba T64000) were measured using a 785 nm Ar laser. X-ray photoelectron spectroscopy (XPS spectra) was recorded from using ESCA+ Omicron Nano Technology, and analyzed using CasaXPS (Casa Software).

2.3.2 Atomic Force Microscopy

A Cr/Pt coated tip (ANSCM-PT, AppNano) was used to measure sample surface roughness (contact mode) and electromechanical coefficients on a Bruker Dimension-ICON atomic force microscope. Inbuilt lock-in amplifiers were used in contact-mode pulsed DC piezo response force microscopy (PFM) to minimize electro-

static effects [68] while detecting the amplitude of displacement of the cantilever tip (excited at ~ 35 kHz). At unity amplifier gain, a first harmonic amplitude of the displacement (FHA_D) of the tip is estimated using the Eq. (2.1):

$$FHA_D = \frac{z_{tip}}{|V_{tip}|} \equiv \frac{s_d A_1}{V_{AC,tip}} \tag{2.1}$$

,where s_d is the deflection sensitivity (~ 126 nm/V, from force curve calibration data for the tip), A_1 is the measured amplitude of the voltage signal of the PFM detector [65], $V_{tip} = V_{AC,tip}\cos(\omega t)$ is the drive amplitude (DA) voltage applied to the tip with respect to the thin film (sample). Measurements in the range $[-10, +10]$ V repeated over three locations in the active area (Fig. (2.8(a))) resulted in trace (forward) and retrace (reverse) scan signals, which have been used to examine the effect of local poling and hysteresis in tip-sample contact region [49, 69]. We note that conventional measurements of electromechanical coefficient d_{33} typically involve device surface areas significantly higher than those accessible in a piezoelectric force microscopy measurement. Well-known electrostatic interactions [70] between the tip and sample can further complicate the analysis. For high drive amplitudes (~ 8V), nonlinear effects [65] are expected to affect the measurement.

2.3.3 COMSOL Simulation

Implementation method

For electromechanical simulations, COMSOL Multiphysics 5.5 (COMSOL Inc) with the MEMS module (under Electrical) was used with piezoelectric and electrostatic effects included. Using stationary analysis, the tip bias is swept from −10 V to +10 V, ignoring sample heating and transient effects. The workflow for the COMSOL simulations has been illustrated in Fig. (2.1).

Module setup

The Solid Mechanics Module is set up from the COMSOL library based upon the linear elastic nature of the materials involved. Silicon wafer (500 μm) coated with Tungsten (50 nm) as the bottom conductive electrode and the conductive PFM tip (tip diameter 20 nm) constitute as the linear elastic materials in this system. The piezoelectric material (100 nm KNN thin film) properties were defined under structural mechanics with a global coordinate system, and the material properties are listed in Table. (2.2). The model used the piezoelectric

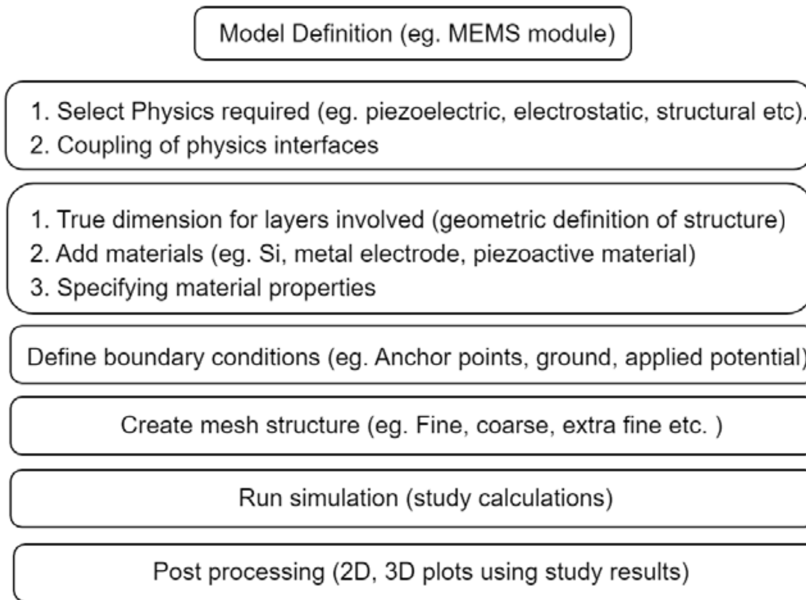

Figure 2.1: COMSOL workflow for the simulations.

material properties under the strain-charge constitutive relation as the governing equations to calculate and simulate the thin film's behaviour (total surface displacement).

The model performs a static analysis of the tip-sample interaction where the electric field ($-10\,\text{V}$ to $+10\,\text{V}$) is applied perpendicular to the surface of the thin film via the PFM tip (cantilever tip as terminal and the tungsten as ground). The total surface displacement of PFM tip simulated using COMSOL is shown in Fig. (2.2). The PFM tip contains a flexible end (cantilever) and a stationary end, and abounded substrate to replicate the real-time measurements. The applied bias of $-10\,\text{V}$ was applied that resulted in the positive z-direction motion (pm) of tip represented by a color bar on the right.

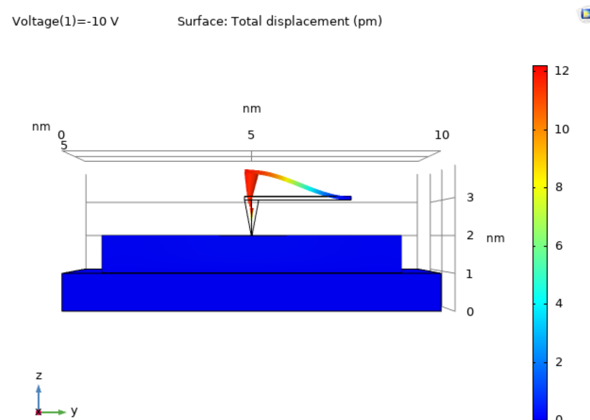

Figure 2.2: Total surface displacement of PFM tip simulated using COMSOL. The PFM tip contains a flexible end and a stationary end bounded to replicate real time measurements. The applied bias of $-10\,\text{V}$ was applied that resulted in the positive z-direction motion (pm) of tip represented by a color bar on the right.

Table 2.2: KNN material properties [71, 72, 73, 74] used for modeling and simulation in COMSOL.

Property	Symbol	Type	Value	Unit	Matrix size
Density	ρ	Isotropic	3460	kg/m^3	1
Relative permittivity	$\varepsilon_{11}^T/\varepsilon_0$ $\varepsilon_{11}^T/\varepsilon_0$	Isotropic	21.0	–	3×3
Piezoelectric charge constant	d_{33} $d_{31}=d_{32}$ $d_{15}=d_{24}$	Symmetric	70.0 -20.0 30.0	10^{-12}C N^{-1}	3×6
Compliance	s_{11}^E s_{12}^E s_{13}^E s_{33}^E s_{44}^E s_{66}^E	Symmetric	14.0 -11.7 -0.2 7.5 12.8 14.0	$10^{-12}m^2/N$	6×6
Elasticity	c_{11}^E c_{12}^E c_{13}^E c_{33}^E c_{44}^E c_{66}^E	Symmetric	0.220 0.183 0.046 0.067 0.077 0.072	$10^{-12}N/m^2$	6×6

2.4 Material Characterization

2.4.1 Calcinated Powder

Calcined KNN (50:50) powder (at 750 °C) was analyzed for its phase purity, phase identification, and compositional analysis using power x-ray powder diffraction (PXRD). The PXRD pattern of as synthesized (amorphous), calcinated, and a reference KNN (JCPDS-00-061-0315) are shown in Fig. (2.3 (b-d)). PXRD pattern of calcined compound reveals sharp and high intensity peaks in good agreement with the reference data. Crystal structure derived from XRD reveals lattice lengths a=3.97 Å, b=5.66 Å, c=5.69 Å, in an orthorhombic structure of calcinated KNN depicted in Fig. (2.3 (e)).

2.4.2 Elemental Analysis

As reported in literature, excess [K^+] is often used in synthesis to account for the expected loss of potassium ions due to their known greater volatility (compared to Na^+) [67, 56] in sol-gel KNN. Elemental composition

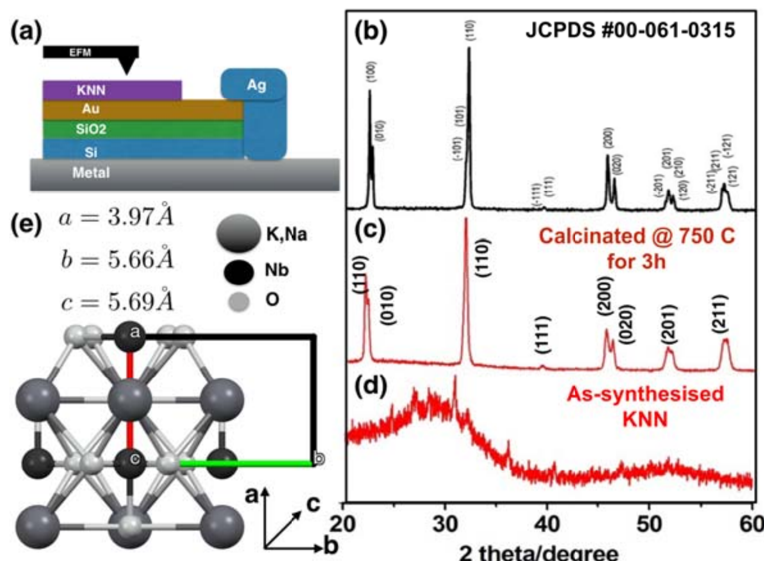

Figure 2.3: (a) Schematic of PFM measurement, (b-d) XRD data of un-annealed and annealed (at 750 °C) KNN, (e) KNN unit cell.

Table 2.3: Stoichiometric composition of as deposited ($K_xNa_{1-x}NbO_3$ or KNN) layers with x=0.3, 0.5 and 0.7, respectively. 'A' denotes total A-site occupation (A=K+Na). Errors in EDX data are estimated to be ∼ 2% (based on bulk samples for this tool).

x	Thickness (nm)	Composition: EDX and (XPS)		
		K/A	Na/A	Nb/A
0.3	62 ± 4	0.365 ±2% (0.3375)	0.634 ±2% (0.6624)	1.036 ±2% (1.028)
0.5	70 ± 2	0.510 ±2% (0.5091)	0.489 ±2% (0.4910)	0.937 ±2% (1.037)
0.7	68 ± 2	0.718 ±2% (0.7682)	0.281 ±2% (0.2317)	0.928 ±2% (1.153)

of the thin films, expressed as ratio y/A (y=K,Na,Nb, and A=(K+Na)), which represents the ratios of each of the metals in A-sites, are examined using EDX and XPS measurements (Table 2.3). Though a slight excess (∼ 4 mol%) in precursor ratios was employed, our results are in close agreement with the precursor ratios, owing to the low temperature of deposition and subsequent drying process. In addition to the presence of the aforementioned, and the oxygen expected in the niobate, other elements such as carbon, platinum, and silicon signals were also detected in EDX(XPS) data. The source of these elements can be attributed to either unreacted precursors, solvent residuals (hydrocarbons), and substrate material (Pt/Si).

The XPS survey in Fig. (2.4) provides the stoichiometric information as well as consistency for different KNN ratios employed here [75]. Fig. (2.4(a)) represents the overall composition of the thin film, whereas the Fig. (2.4(b)) and Fig. (2.4(c)) represents the variation in K:Na, where the peaks for Sodium and Potassium are in agreement with the K:Na ratios = 30 : 70, 50 : 50, and 70 : 30, respectively. An increase in peak intensity represents the increase in K^+ content and a reduction in peak intensity represents the lowering of Na^+ content

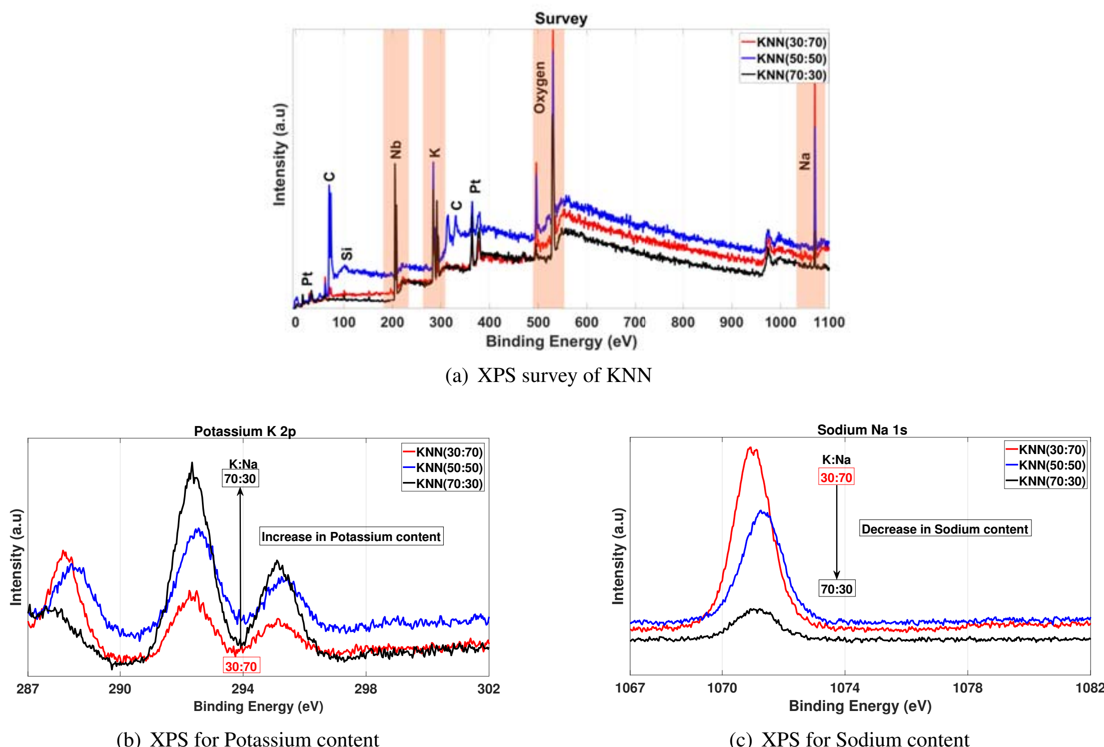

(a) XPS survey of KNN

(b) XPS for Potassium content

(c) XPS for Sodium content

Figure 2.4: XPS spectra for $K_xNa_{1-x}NbO_3$ layers with x=0.3, 0.5, and 0.7 respectively (the solid colored blocks are drawn as aid for the eye to elements of attention).

in the $K_xNa_{1-x}NbO_3$ system. The stoichiometric ratios were also examined by the area under the curve and are listed in Table. 2.3.

The quantitative elemental ratio is relative to the presence of ‘y’ (y=K, Na, Nb) to ‘A’ (A=(K+Na)). In addition to the presence of ‘y’, other elements such as carbon, oxygen, platinum, and silicon were also present in a small amount. The source of these elements can be traced/attributed to either unreacted precursors, solvent residuals (hydrocarbons), atmospheric gases (carbon/oxygen), and substrate material (Pt/Si) as seen in Fig. (2.4(a)).

2.4.3 Thin Film Characterization

XRD data (Fig. (2.5)) for KNN thin films on tungsten substrates are in agreement with published data for amorphous KNN [76]. A Cr/Pt coated tip (ANSCM-PT, AppNano) was used to measure sample surface roughness (contact mode) and electromechanical coefficients on a Bruker Dimension-ICON atomic force microscope. Surface roughness (extracted as an RMS of height scan) ($\sim$ 16 nm to 50 nm) of the deposited KNN thin films (Fig. (2.5)) was averaged over a scan area of 5x5 μm^2. The high surface roughness can be attributed to solvent removal during the drying process.

The reduction in excited state populations (Fig. (2.6)) in vibrational modes V1, V2 and V5 [59] can be

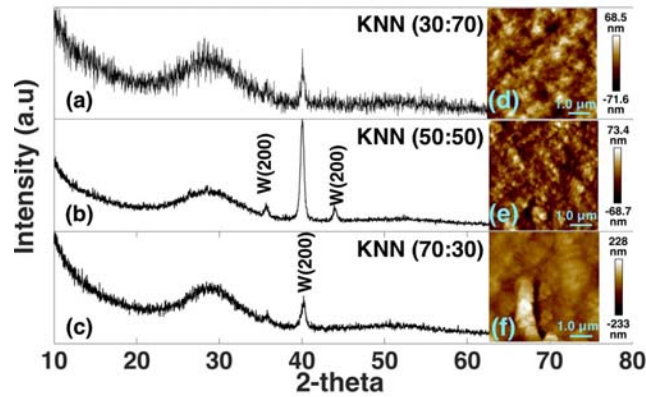

Figure 2.5: X-ray diffraction data ((a), (b), and (c)) for thin films of KNN (K:Na ratios = 30:70, 50:50 and 70:30). Substrate (W) peaks are indicated. Surface roughness (RMS) for these compositions are measured to be ∼ 16.5 nm, 15 nm, and 48.3 nm, respectively, in the corresponding AFM scans ((d), (e), and (f)).

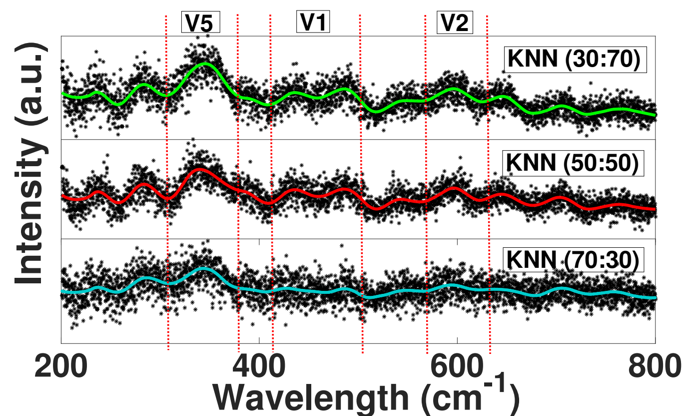

Figure 2.6: Raman spectra for $K_xNa_{1-x}NbO_3$ layers with x=0.3, 0.5, and 0.7 respectively (the solid colored lines are drawn as aid for the eye).

possibly attributed to a stronger distortion of the short-range lattice with rising K^+ content and applied stress, resulting in more pronounced charge separation. However, the simplistic monotonic behavior that may be expected from composition-dependent lattice distortion alone is modified by the presence of morphotropic phase boundaries (MPBs) at x=0.31 and 0.48. Domain reversal at coercive voltage for all compositions appears to occur near −2 V, with wider hysteresis for x=0.5, which is suggestive of the presence of an MPB near that composition [56, 59]. As Na^+ concentration increases, its relatively smaller ionic radius (∼ 1.39 Å) may permit a greater degree of freedom for distortion of the lattice. These phases may thus exhibit lower energy of interconversion due to effect of local stress between grains with different phases and reduction of activation energies of conversion due to mechanical effects [58]. Nearly amorphous KNN layers can act as precursors to formation of composition dependent mixtures of cubic (C), tetragonal (T), and orthorhombic (O) phases upon annealing, with an impact on the emergent piezoelectric properties of KNN [56].

The KNN lattice is expected to be non-centrosymmetric when piezoelectrically active [77]. The V5 vibra-

tional mode corresponds to an enhanced degree of freedom of lattice distortion around the symmetrical axis of the central Nb atom, which may be expected to lead to higher excited state populations, resulting in stronger Raman Stokes lines [77]. Further, the peak of the V5 vibrational mode is shifted and slightly broadened in the x=0.5 sample, due excess K^+, which is correlated to lattice distortion. V1 and V2 vibrational modes are stretching modes related to A-site atoms (K/Na) [59]. The splitting of V1 and V2 mode into two shoulders is related to the freedom of motion of Na^+ ion. For the V1 mode, the x=0.5 sample has sharper peaks shifted towards lower wavenumbers, corresponding to energy stabilization discussed above.

2.5 Piezo Response Force Microscopy

The morphology, surface roughness, electromechanical coefficient (d_{33}) and piezo-response of deposited thin films were examined using Bruker's Dimension icon. The SPM probe used was ANSCM-PT from APPNANO Cr/Pt coated tip. The tip radius was t_r ~20 nm, resonance frequency f~43 kHz to 81 kHz, and spring constant k~1 N/m to 5 N/m. For morphology and roughness measurements, tapping mode was used, and for piezo-response microscopy, contact mode was employed (optimized vertical mode). The data acquired via photo-detectors and piezo-signal or displacement amplitude was processed via built-in lock-in amplifiers. Using piezo-response force microscopy (PFM) at/near-resonant frequency can lead to abrupt changes in phase lag between the excitation signal and the piezoresponse. Thus, operating near the resonance (~43 kHz) can potentially make it harder to detect measurable quantities such as domain polarization and strength of electromechanical response (~ amplitude, z), due to artefacts arising from strong intrinsic cantilever excitation [70]. We have carried out our measurements at 35 kHz to avoid this issue (experimentally determined resonant frequency of the tip-sample system ~ 43 kHz) as shown in Figure (2.7).

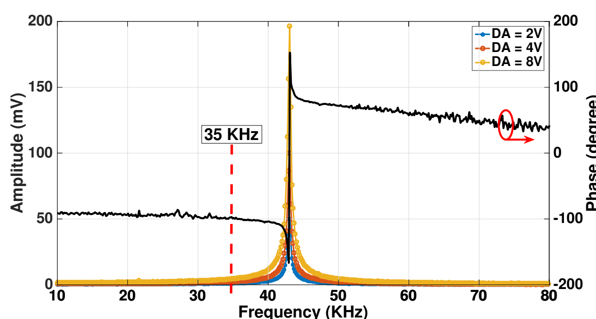

Figure 2.7: Amplitude and Phase vs excitation frequency of SPM cantilever near resonance and its voltage dependence response. Marked frequency of operation 35 kHz.

Using piezo-response force microscopy (PFM) at/near resonant frequency can lead to steep changes in

phase lag between the excitation signal and the piezo response. Thus, operating near the resonance (~43 kHz) can potentially make it harder to detect measurable quantities such as domain polarization, shown in Fig. (2.8(a)) (proportional to the phase lag), and strength of electromechanical response (~ amplitude, z), due to artifacts arising from strong intrinsic cantilever excitation [70]. We have carried out our measurements at 35 kHz to avoid this issue (experimentally determined resonant frequency of the tip-sample system ~ 43 kHz). Elimination of such tip resonance effects at low amplification results in the observed thin film piezo response (Eq. (2.1)) in the form of characteristic *butterfly* curves for each of the studied stoichiometric ratios of K:Na (Fig. (2.8(b))).

This measurement exhibits expected polarization switching and phase reversal at voltages corresponding to the coercive voltage for all three compositions. Further, the dependence of the piezo response on the drive amplitude (observed to be linear for low drive amplitudes) for the sample with the highest tip displacement (K:Na=1:1) (Fig. (2.9)) exhibits a broadening of the butterfly curve. The measured displacement was found to be very low for x=0.3 and x=0.7 for DA=2, 4, and 6V respectively. As a result, we carried out a high drive amplitude measurement at 8V to obtain estimates of possible FHA_D values (Eq. (2.1)) as shown in Fig. (2.8(b)). Results with these extremal values (Fig. (2.8(c))) exhibit pronounced hysteresis for x=0.5 (KNN (50:50)). Simulations of the tip-sample system for a KNN thin film with d_{33} ~ 46 pC/N [78] (Fig. (2.9)) yield displacements of the SPM tip in near agreement of the performed PFM experiments, suggesting that electrostatic effects play a weak role with tip diameters ~ 10 nm for low tip-biases, and that electromechanical response of the film is primarily responsible for accounting for the observed deflections in that regime. Induced poling and film expansion effects expected for positive tip biases may play a role in affecting the linearity of the response.

In literature, the morphotropic phase boundary (MPB) is reported to occur at K:Na= 48 : 52, with some reports extending that composition to as high as 52 : 48 [36]. The observed FHA_D values at V_{DC} = 0 and 10V (Figure (2.8(c))), respectively, are maximized for the 50 : 50 (x = 0.5) sample with a simultaneous maximum value for the coercive voltage, which suggests the presence of an MPB at or near that composition. Induced strain in KNN thin films has been associated with enhanced electromechanical coefficients [51]. The forward trace in applied DC voltage poles the sample locally [79], with hysteresis manifested in the form of a non-zero coercive voltage, V_c. Some studies have been suggestive of the potential role of high electric fields in inducing phase transformations in the KNN system, and other systems [49]. The high values of FHA_D observed in the absence of any aggressive thermal treatment suggests that it may be possible to induce piezoelectrically

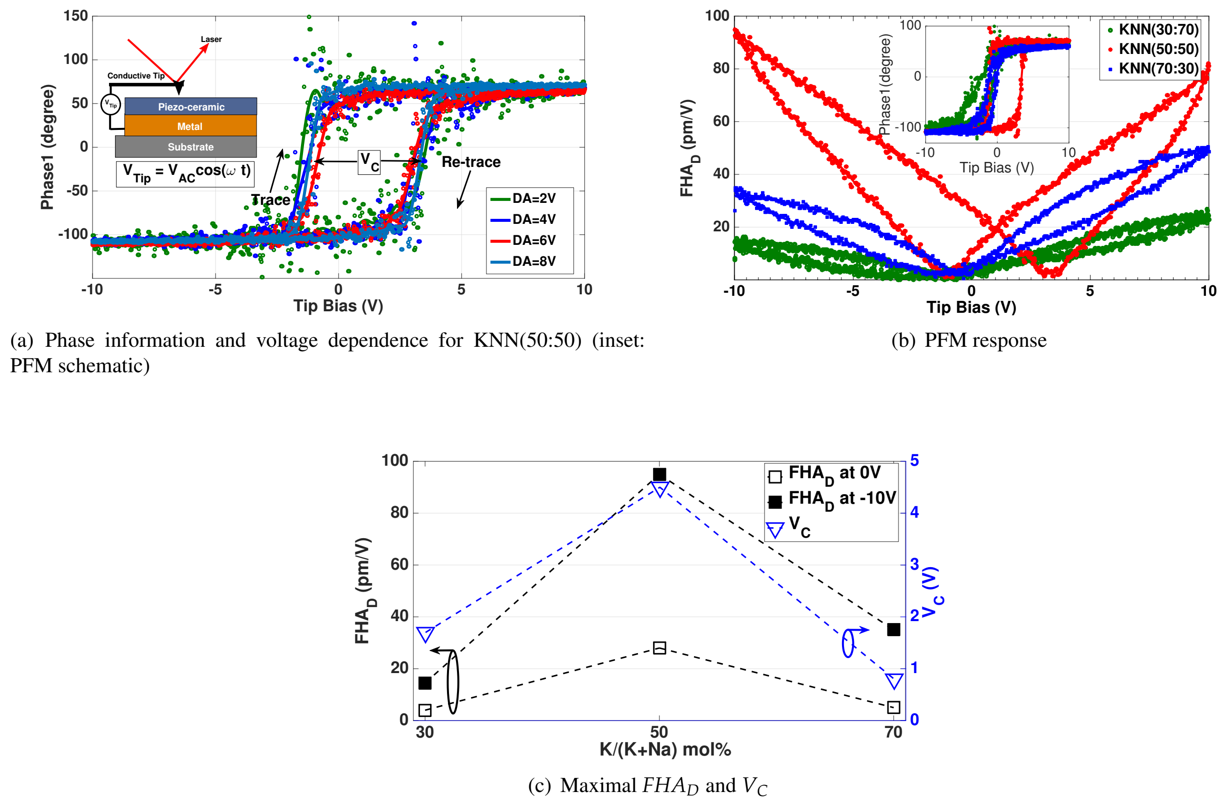

(a) Phase information and voltage dependence for KNN(50:50) (inset: PFM schematic)

(b) PFM response

(c) Maximal FHA_D and V_C

Figure 2.8: (a) Phase information for KNN (50:50) as a function of variable voltage, (b) Stoichiometry dependent piezo-response measurement by PFM for the KNN film with x = 0.3, 0.5, and 0.7 respectively at 8V drive amplitude. Inset: phase vs voltage hysteresis loop, (c) Measured FHA_D values at zero and maximum negative applied DC voltage, and coercive voltage for each composition.

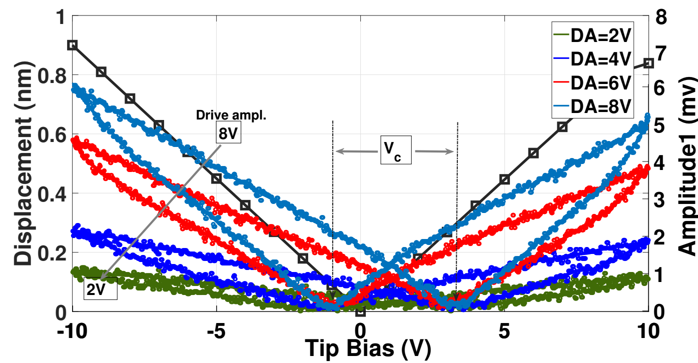

Figure 2.9: PFM (Piezo-response force microscopy) and simulated response (black line with square symbols) for KNN (50:50) thin films.

favorable phases near MPBs in low-temperature unannealed solution-processed thin films under application of very high electric fields (1 MV/cm).

PFM studies for comparably thin films (∼ 70 nm) in other systems [80] have found reversible and irreversible switching of domains under poling. However, the high values of FHA_D achieved under application of very high and intense electric fields may not correspond to achievable d_{33} coefficients in larger area devices poled using conventionally sized contacts [49]. Accordingly, No attempt is made in this study to claim large electromechanical coefficients at this stage of the work, since there is considerable disagreement in literature regarding the suitability of piezoelectric force microscopy [81] as a definitive measurement for d_{33} (estimated 70 pC/N for the unity ratio composition), owing to contact area [82] and electrostatic effects [70].

2.6 Thermal Budget

Thermal budget defined as the total amount of thermal energy transferred or required for the fabrication of a device [83] in terms of elevated temperature requirement, the time duration of high temperature and kind of heat treatment (conventional or non-conventional). In general, a low thermal budget is required in IC manufacturing due to a different type of materials involved in terms of thin films. Low thermal budget can also facilitate the use of non-traditional substrates for film deposition and device fabrication such as PET or plastics and reduces the overall fabrication cost. To capture the full thermal impact of the processes, we have estimated the thermal budget [83] of each report using the expression, $\Sigma_{k=1}^{k=N} \Delta t_k T_k$, where for an N step process, the time of each step (Δt_k) and the temperature of that step (T_k) is accounted in this figure of merit and is shown in Table. (2.4). However, if we consider the thermal budget of the process, we can report a figure of 0.90 °C min, which is the lowest calculated value for recent KNN synthesis literature.

2.7 Summary

We have detected large piezoelectric forces in unannealed room-temperature processed KNN thin films using PFM measurements. The results compare favorably with published literature [48] on solution-deposited KNN , especially given that we are able to achieve crack-free uniform films with a single sol deposition step. Material characterization data suggest that composition plays a strong role in the piezo response, due to the presence of MPBs. This picture is expected to be further complicated by the presence of grain boundaries, size and density variations, etc. in practical devices. Such processes may be suitable for the development of high

Table 2.4: Comparison of elctro-mechanical coefficients using various deposition and characterization techniques. To capture the full thermal impact of the processes, we have estimated the thermal budget[83] of each report using the expression, $\Sigma_{k=1}^{k=N}\Delta t_k T_k$, where for an N step process, the time of each step (Δt_k) and the temperature of that step (T_k) is accounted in this figure of merit. LSV=Laser Scanning Vibrometry. BC=Berlincourt method.

Deposition technique	d_{33} (pC/N)	Measurement Technique	Estimated thermal budget (k°C· min)
Electrophoretic [39]	40	BC	234.00
Sputtered [38]	45	PFM	144.00
Hydrolic press [84]	71	BC	126.00
Ball milled [48]	18	BC	84.00
Drop-cast [85]	35	PFM	72.00
Spin-coat [78]	46	PFM	39.00
Spin-coat [42]	40	PFM	23.75
Spin-coat [86]	35	LSV	8.70
Spin-coat [87]	56	LSV	8.20
Spin-coat (this work)	~70	PFM	0.90

performance energy harvesters, and transducers for sensor applications on low-cost flexible substrates[88]. Further work is needed to elucidate the precise relationship between achieved FHA_D values, the applied strain at the grain boundaries at nanoscale, and the external electric field. Given the known uncertainties in PFM measurements, in future work, we also plan to examine capacitive measurements to derive reliable measures of electromechanical coefficients for KNN, and effective densification of KNN thin films using in-plane electric fields during processing of the films.